

***CLOUDS, PRECIPITATION AND MARINE
BOUNDARY LAYER STRUCTURE DURING THE
MAGIC FIELD CAMPAIGN***

Xiaoli Zhou¹, Pavlos Kollias¹, and Ernie R. Lewis²

1. Department of Atmospheric and Oceanic Sciences, McGill University,
Montreal, CA
2. Biological, Environmental & Climate Sciences Department, Brookhaven
National Laboratory, Upton, NY

Corresponding author: Xiaoli Zhou
Department of Atmospheric and Oceanic Sciences
Montreal H3A0B9 Quebec, Canada
email: xiaoli.zhou@mail.mcgill.ca

*Accepted for publication in
the Journal of Climate*

April 2014

Biological, Environmental & Climate Science Dept.

Brookhaven National Laboratory

**U.S. Department of Energy
DOE Office of Science**

Notice: This manuscript has been authored by employees of Brookhaven Science Associates, LLC under Contract No. DE-SC0012704 with the U.S. Department of Energy. The publisher by accepting the manuscript for publication acknowledges that the United States Government retains a non-exclusive, paid-up, irrevocable, world-wide license to publish or reproduce the published form of this manuscript, or allow others to do so, for United States Government purposes.

DISCLAIMER

This report was prepared as an account of work sponsored by an agency of the United States Government. Neither the United States Government nor any agency thereof, nor any of their employees, nor any of their contractors, subcontractors, or their employees, makes any warranty, express or implied, or assumes any legal liability or responsibility for the accuracy, completeness, or any third party's use or the results of such use of any information, apparatus, product, or process disclosed, or represents that its use would not infringe privately owned rights. Reference herein to any specific commercial product, process, or service by trade name, trademark, manufacturer, or otherwise, does not necessarily constitute or imply its endorsement, recommendation, or favoring by the United States Government or any agency thereof or its contractors or subcontractors. The views and opinions of authors expressed herein do not necessarily state or reflect those of the United States Government or any agency thereof.

25 **Abstract**

26

27 The recent ship-based MAGIC field campaign with the marine-capable Second ARM
28 Mobile Facility (AMF2) deployed on the Horizon Lines cargo container M/V *Spirit*
29 provided nearly 200 days of intra-seasonal high-resolution observations of clouds,
30 precipitation and marine boundary layer (MBL) structure on multiple legs between Los
31 Angeles, California, and Honolulu, Hawaii. During the deployment, MBL clouds
32 exhibited a much higher frequency of occurrence than other cloud types and occurred
33 more often in the warm season than in the cold season. MBL clouds demonstrated a
34 propensity to produce precipitation, which often evaporated before reaching the ocean
35 surface. The formation of stratocumuli is strongly correlated to a shallow MBL with a
36 strong inversion and a weak transition, while cumuli formation is associated with a much
37 weaker inversion and stronger transition. The estimated inversion strength (EIS) is shown
38 to depend seasonally on the potential temperature at the 700 hPa. The location of the
39 commencement of systematic MBL decoupling (DE) always occurred eastward of the
40 locations of cloud breakup (CBs), and the systematic decoupling showed a strong
41 moisture stratification. The entrainment of the dry warm air above the inversion appears
42 to be the dominant factor triggering the systematic decoupling, while surface latent heat
43 flux, precipitation and solar radiation did not play major roles. MBL clouds broke up over
44 a short spatial region due to the changes in the synoptic conditions, implying that in real
45 atmospheric conditions, the MBL clouds do not have enough time to evolve as is in the
46 idealized models.

47

48

49

50 **1. INTRODUCTION**

51

52 On average, near 30% of the global oceans are covered with low-level clouds (ISCCP
53 online data set: <http://isccp.giss.nasa.gov/climanal7.html>). These prevailing marine
54 boundary layer (MBL) clouds are a key component in the earth's radiation budget, from
55 which Stratocumulus (Sc) clouds exert a strong negative net radiative effect due to their
56 low height and high areal coverage, by strongly reflecting incoming solar radiation but
57 only weakly influencing the outgoing longwave radiation (Wood, 2006). Cumulus (Cu)
58 have a reduced effect on the radiation due to their low areal coverage (Wood, 2006;
59 Karlsson et al. 2010) but play a critical role in the vertical redistribution of moisture and
60 energy in the lower troposphere (Tiedke et al., 1988). Thus, it is important for global
61 climate models to accurately represent these cloud regimes.

62 The evolution, with increasing sea surface temperature (SST), from Sc regimes to Cu
63 regimes in the trade wind regions and then eventually to congestus and deep convective
64 Cu over the warmer waters of the intertropical convergence zone are well documented
65 (e.g., Albrecht et al., 1995a,b; Karlsson et al., 2010). An inversion layer that is often
66 thought of as the top of the MBL typically caps the Sc. A regime with Cu-under-Sc
67 usually occurs during the progression between Sc and Cu and is associated with a weakly
68 stable layer below the inversion base that is characterized by a sharp decrease of moisture
69 with height (e.g. Krueger et al. 1995; Bretherton and Wyant, 1997; Jones et al. 2011).

70 This stable layer, referred here as the transition layer, separates a region below of surface
71 flux-driven turbulence from a region above dominated by radiatively driven convection
72 (Bretherton and Wyant, 1997) and acts to isolate the upper MBL from the surface
73 moisture supply. When this vertical moisture stratification gets sufficiently strong,
74 systematic decoupling occurs, and remains decoupled with further increase in SST. This
75 systematic decoupling is a crucial first step in the Sc-to-Cu transition and is not affected
76 by the diurnal cycle of radiation (Wyant et al. 1997).

77 Due to the lack of fully understanding of the mechanisms responsible for the evolution of
78 MBL structure and cloud, global weather and climate prediction models still do not
79 accurately reproduce the evolution between these cloud regimes, and the locations of Sc
80 breakup and the rates of change of cloud coverage vary widely among different models,
81 which generally underestimate cloud amounts in the Sc region while overestimating them
82 in the Cu region (Teixeira et al., 2011).

83 One of the main factors hindering progress in representing these clouds in numerical
84 models has been the lack of observational data. Most of the observational data sets used
85 to evaluate the cloud-related processes are satellite-based. Satellite data have proven
86 valuable in determining the climatological links between MBL inversion base height
87 (MBLH) and cloud cover (e.g. Heck et al. 1990; Wang et al. 1993; Wood and Bretherton,
88 2004). However, satellite observations cannot provide information on detailed vertical
89 cloud and thermodynamic structure of the MBL especially during decoupling conditions
90 (Wood and Bretherton, 2004; Kalsson et al. 2010). The difficulty in accurately observing
91 low-level clouds with small-scale variability (Xu and Cheng, 2013) further restricts the
92 applicability of satellite data in the understanding of the transition between these cloud

93 regimes.

94 In addition to satellite data, several field campaigns have been conducted to study MBL
95 clouds and the mechanisms responsible for the Sc-to-Cu transition. These previous ship-
96 based efforts provided a wealth of information with regard to the vertical structure of the
97 MBL and associated clouds. However, they were primarily conducted in a fairly small
98 region and focused on studying one specific cloud type. For example, the First
99 International Satellite Cloud Climatology Project (ISCCP) Regional Experiment (FIRE;
100 Albrecht et al. 1988) focused on Sc and cirrus cloud regimes, the Tropical Instability
101 Wave Experiment (TIWE; Albrecht et al. 1995b) focused on the trade wind Cu boundary
102 layer structure, and during the Atlantic Stratocumulus Transition Experiment (ASTEX;
103 Albrecht et al., 1995a) a transition region in which Cu form beneath Sc was observed.
104 Albrecht et al. (1995b) compared the large-scale forcing and thermodynamic profiles
105 from these three field experiments and concluded that the increase in sea surface
106 temperature (SST) is important in the thinning of the Sc. The same study provided
107 evidence that the boundary layer structure and the associated transition from Sc to Cu
108 may be more complicated than originally thought. More recently, Jones et al. (2011)
109 examined in detail the coupled and decoupled boundary layers in the Variability of the
110 American Monsoon Systems (VAMOS) Ocean-Cloud-Atmosphere-Land Study Regional
111 Experiment (VOCALS-REx; Wood et al., 2011). One of the major findings in Jones et al,
112 2011 is that the difference between MBLH and the lifting condensation level (LCL) best
113 predicts decoupling.

114 Previous numerical studies have demonstrated that the systematic decoupling is mainly
115 driven by the increasing surface latent heat flux (LHF) as a response to the increasing

116 entrainment due to the warmer SST (e.g. Bretherton and Wyant, 1997, Sandu and Stevens,
117 2011). The subsequent Sc breakup was explained as a result of the further increase of the
118 SST that causes the Cu to become deeper and more vigorous, penetrating farther into the
119 inversion and entraining more dry air from above the inversion (Wyant et al., 1997;
120 Sandu and Stevens, 2011). Although numerical studies have advanced our knowledge of
121 MBL structure and clouds, simulations have usually simplified the problem by assuming
122 the constant divergence and free-tropospheric lapse rates (Bretherton and Wyant, 1997),
123 but neither assumption is supported by observations.

124 There are noticeable discrepancies between idealized model simulations and
125 observational findings. For instance, the dominant effect of the LHF on MBL decoupling
126 was not observed in VOCAL-REx (Jones et al. 2011). Additionally, the assumption of a
127 constant free-atmosphere lapse rate might introduce biases because MBLH and boundary
128 layer mixing ratios are very sensitive to above-inversion features (Albrecht 1984;
129 Krueger et al. 1995). At the same time, the availability of comprehensive, long-term
130 observations that document the gradual MBL decoupling and Sc-to-Cu transitions is
131 limited.

132 The recent MAGIC field campaign provided high resolution, profiling observations, from
133 the coast of California to Honolulu for over 200 days. The collected dataset is the most
134 extensive direct, long-term, intra-seasonal set of measurements of MBL structure and
135 cloud evolution from Sc to Cu over large downwind regions. Here, we investigate the
136 potential of the dataset in advancing our understanding of the systematic MBL
137 decoupling and Sc breakup to be compared with and constrain the modeling studies.

138 The remaining of the manuscript is organized as follows. Brief descriptions of the
139 MAGIC field campaign and of the AMF-2 instruments are provided in Section 2, and the
140 methodology used for this study is introduced in Section 3. Results are presented in
141 Section 4, and a summary of these results and plans for future work are presented in
142 Section 5.

143

144 **2. OBSERVATIONS**

145

146 2.1 The MAGIC Field Campaign

147 The MAGIC field campaign (<http://www.arm.gov/sites/amf/mag/>) deployed the US
148 Department of Energy (DOE) Atmospheric Radiation Measurement (ARM) Mobile
149 Facility 2 (AMF2) on the commercial cargo container Horizon *Spirit* (Fig. 1a). The
150 MAGIC transect is very near the line from the coast of California to the equator (35°N,
151 125°W to 1°S, 173°W) that was chosen by modelers to compare model results for the
152 Global Energy and Water Experiment (GEWEX) Cloud System Studies (GCSS) Pacific
153 Cross-section Intercomparison (GPCI) study, in which more than twenty climate and
154 weather-prediction models participated (Teixeira et al., 2011). Thus, MAGIC with its
155 unprecedented, intra-seasonal, high-resolution ship-based observations is expected to
156 provide constraint, validation, and support for the aforementioned modeling efforts and at
157 the same time contribute in improving our understanding of the Sc-to-Cu transition along
158 this GPCI transect.

159 From October, 2012 through September, 2013, the *Spirit* completed 20 round trips
160 between Los Angeles, California, and Honolulu, Hawaii. Each trip is called a “leg”, and
161 legs are numbered sequentially as “LegxxA” for the trips from Los Angeles to Honolulu
162 and “LegxxB” for the return trips (Fig. 1b). During the legs from Los Angeles, the *Spirit*
163 traveled at ~21 kts ($\sim 10.5 \text{ m s}^{-1}$) and covered the 4100 km distance in 4.5 days. The *Spirit*
164 returned to Los Angeles at ~16 kts ($\sim 8 \text{ m s}^{-1}$), making the trip in approximately 6.5 days
165 (the lower speed resulting in lower fuel costs and allowing the ship to remain on a two-
166 week schedule; Lewis et al., 2012). The departure and arrival times of MAGIC legs are
167 listed in Appendix A. Two technicians associated with the MAGIC campaign lived on
168 board the *Spirit* during the deployment to maintain the instrumentation, launch
169 radiosondes, and perform other tasks.

170

171 2.2 AMF2 instrumentation and data description

172

173 The AMF2 contains a state-of-the-art instrumentation suite and was designed to operate
174 in a wide range of climate conditions and locations, including shipboard deployments.
175 The AMF2 was located on the bridge deck of the *Spirit*, approximately 16 m above sea
176 level (ASL). The primary AMF2 instruments used in the current study are 1) a Ka-band
177 ARM Zenith Radar (KAZR), 2) a laser ceilometer, 3) a Vaisala weather station, 4) a
178 inertial navigational location and attitude system (NAV), 5) the Marine Meteorological
179 System (MARMET) installed on the mast of the *Spirit* approximately 27 m above sea
180 level and an Infrared Sea-surface temperature Autonomous Radiometer (ISAR), and 6)

181 radiosondes (four or eight per day). AMF2 also contained a motion-stabilized W-band
182 radar, a radar wind profiler, a broadband and spectral radiometer suite, aerosol
183 instrumentation, and other instruments. The operational status of all instruments during
184 the campaign is summarized in Appendix B. There were some time periods when the
185 KAZR was not acquiring data for various reasons (e.g., installation, power outages, etc.),
186 but KAZR measurements were obtained for all of Leg03A through Leg08B, Leg11, and
187 Leg14A through Leg17B. The analyses presented here are based on these data, in total 22
188 transits between California and Hawaii through the Sc-to-Cu transition region comprising
189 more than 3000 hours. The data are separated into two seasons, the warm season: Leg11
190 and Leg14 to Leg17 (May 25 to June 6, and July 7 to August 29, 2013), and the cold
191 season: Leg03 to Leg08 (October 6 to December 27, 2012).

192

193

194 2.2.1 Ka-band ARM Zenith Radar (KAZR)

195

196 The KAZR, formerly known as the millimeter wavelength cloud radar (MMCR, Moran et
197 al., 1998), is a 35-GHz profiling Doppler radar that retrieves information on the vertical
198 distribution of the hydrometeors in the atmospheric column. Due to its short wavelength
199 (8.6 mm), the KAZR has sufficient sensitivity to detect MBL clouds with little
200 attenuation under moderate drizzle conditions. The KAZR might fail to detect very thin
201 liquid clouds and it can provide inaccurate hydrometeor-layer heights during heavy
202 precipitation because of severe radar signal attenuation (Matrosov, 2007), but because a
203 ceilometer was used (Section 2.2.2) and because there was very little heavy precipitation

204 during MAGIC, these issues should have little effect on the results of this study. The
205 KAZR utilizes a new digital receiver that provides higher temporal (less than 2 s) and
206 spatial (30 m) resolution than the MMCR (Widener et al., 2012). It is unaffected by
207 Bragg scattering and has small antennas with narrow beamwidths as well as limited
208 sidelobes (Kollias et al., 2007). During MAGIC, the KAZR was configured to have
209 temporal resolution of about 0.4 s to oversample the ship motion, thus enabling
210 compensation of the effects of this motion on the radar observables during data post-
211 processing. In this study, all KAZR measurements have been averaged over 4 s, which
212 allows for the detection of small-scale Cu.

213

214 2.2.2 Ceilometer

215

216 A ceilometer (Vaisala model CT25K) operating at a wavelength of 910 nm was used to
217 detect the base heights of clouds. The ceilometer's range resolution was 10 m, and its
218 temporal resolution was near 16 s for Leg03 and Leg04 and 3 s for the other legs. In order
219 to maintain the 4-s temporal resolution, it is assumed that each reported base height is
220 representative of the entire original time period.

221

222

223 2.2.3 Vaisala Weather station

224

225 A Vaisala weather station WXT-520 installed as part of a suite of meteorological
226 instruments associated with the Aerosol Observing System of the AMF2 (AOSMET)

227 measured rain intensity at 1 s resolution which was used to detect the presence of
228 precipitation reaching the ground (see Section 3c).

229

230 2.2.4 Navigational Location and Attitude (NAV)

231

232 NAV provided ship location and attitude with a temporal resolution of 1 s during the
233 period between November 3 and December 3, 2012 (Leg05A to Leg07A), and 0.1 s for
234 the rest of the deployment. As all macroscopic data are averaged over 4 s, both temporal
235 resolutions are sufficiently accurate for the present comparisons.

236

237 2.2.5 Marine Meteorological Measurement (MARMETX) & Marine Flux 238 (MARFLUX) data sets

239

240 The MARMETX data set (<http://www.arm.gov/campaigns/amf2012magic/>) contains
241 standard surface meteorological parameters measured by the MARMET: temperature (T),
242 pressure (P), relative humidity (RH), and apparent and true wind speed and direction; and
243 the sea-surface skin temperature (SSST) measured by the ISAR (with an accuracy of
244 better than 0.1°C). MARFLUX (<http://www.arm.gov/campaigns/amf2012magic/>)
245 contains the surface fluxes of moisture and sensible and latent heat calculated by the
246 TOGA-COARE air-sea flux algorithm (Fairall et al., 1996) using the MARMETX
247 variables. Both MARMETX and MARFLUX have a time resolution of 1 min.

248

249 2.2.6 Atmospheric Soundings

250

251 Standard radiosondes (Vaisala model MW-31, SN E50401) were launched every 6 h to
252 measure vertical profiles of the thermodynamic state of the atmosphere (T, P, RH, and
253 wind speed and direction). During Leg14, which occurred in July 2013, launches were
254 made every 3 h to provide a more detailed picture of the atmospheric structure. Only
255 soundings providing measurements as high as 15 km were used in this study (389 in all).
256 The radiosondes collected data every 2 s during their ascent, providing a typical vertical
257 resolution of 10 m in the troposphere. However, owing to the limited launching frequency
258 (four to eight per day), sounding data can be interpolated to higher-resolution time steps
259 with only limited confidence.

260

261

262 **3. METHODOLOGY**

263

264 **3.1 Hydrometeor mask**

265

266 A hydrometer mask was applied to the raw KAZR reflectivity measurements to identify
267 the radar range gates that contain appreciable returns from hydrometeors. Following
268 Rémillard et al. (2012), this mask uses the algorithm of Hildebrand and Sekhon (1974)
269 and a two-dimensional (time-height) filter to identify the number of hydrometeor layers
270 in the atmospheric column and their corresponding boundaries. The lowest hydrometeor
271 boundary is not necessarily the cloud base because the KAZR cannot distinguish cloud
272 drops from precipitation particles below the cloud base.

273

274 3.2 Cloud boundaries and cloud classification

275

276 To obtain cloud boundaries, the hydrometeor mask is combined with the ceilometer-
277 generated time series of cloud-base height. The ceilometer cloud-base heights are binned
278 to the KAZR spatial resolution, with an uncertainty of less than 15 m (the KAZR has
279 range resolution of 30 m). Examples of the KAZR hydrometeor mask along with first
280 ceilometer-derived cloud-base heights for Leg04A and Leg04B are shown in Fig. 2. The
281 combination of the KAZR and the ceilometer is sufficient to characterize cloud fraction
282 (CF) and layering in the lower troposphere (i.e., $< \sim 3$ km), although hydrometeor
283 occurrence in the upper troposphere is probably underestimated because the maximum
284 operational range of the ceilometer is 5-6 km. However, as the analysis here pertains to
285 MBL clouds, this underestimation should not introduce any biases.

286 Cloud tops for each hydrometeor layer throughout the troposphere are determined using
287 the KAZR-derived hydrometeor mask. In liquid clouds, KAZR reflectivity measurements
288 below the first cloud-base height determined by the ceilometer are used to characterize
289 precipitation (see next section). If no ceilometer data are available, no KAZR data below
290 300 m are used, since they often contain artifacts (especially when no precipitation is
291 present). In cases when the first ceilometer-derived base height is 100 m or more less
292 than the first KAZR-defined hydrometeor base height, the two clouds are considered
293 independent, with the first cloud-top height undetermined; otherwise the first KAZR
294 hydrometeor top is considered to be the first cloud top.

295

296 Once the cloud boundaries are determined, each time-height cluster of KAZR echoes
297 with more than 25 connected pixels (in time-height space) is considered to be a cloud
298 entity. In order to obtain realistic bases of multiple-layer cloud entities, the bases of the
299 second cloud level are further smoothed according to the ceilometer-derived base heights.
300 KAZR echoes below the newly defined cloud bases are neglected. Each cloud entity is
301 categorized into one of four types based on its average base and top heights (Table 1, see
302 Fig. 3a as an example): high-level, mid-level, MBL, or cumulus congestus and deep
303 convective. High-level clouds have average base heights of at least 6 km. Mid-level
304 clouds have average base heights between 3 km and 6 km. MBL clouds have average
305 base heights and top heights less than 3 km, or have undetermined average top heights.
306 Cumulus congestus and deep convective clouds have average base heights less than 3 km
307 but average top heights of at least 3 km. The statistical results of cloud properties
308 presented in this study are not sensitive to the specific values chosen for the thresholds.

309 An MBL cloud layer is detected if more than 10% of cloud bases are measured over a
310 continuous range of heights during one hour (a one-gate gap is allowed). The cloud bases
311 here refer to the first and second ceilometer-derived bases and the first three
312 hydrometeor-mask bases.

313 As the focus of this study is MBL clouds, emphasis is placed on these clouds, which are
314 further divided into three subtypes: stratocumulus (Sc), cumulus (Cu), and indeterminate
315 (e.g., Figs. 3b and 3c). Sc are low clouds composed of an ensemble of individual
316 convective elements that together assume a layered form (Wood, 2012), whereas Cu
317 clouds are separate convective elements. The difference between Sc and Cu in this study

318 is based on their time durations: a cloud is defined as Sc if it lasts more than 20 min, and
319 as Cu if its duration is less than 20 min. Sc clouds are also required to have a narrow
320 cloud top height distribution that is restricted by a specific standard deviation threshold
321 that depends on its duration (see Table 1 for details). The remaining MBL cloud clusters
322 make up the subtype ‘indeterminate’. Because of the limited nature of the MAGIC
323 observations (1D in distance/time and height), these cloud types are not mutually
324 exclusive.

325 Because of their ship-based origin, the cloud macroscopic data for each leg depend on
326 both time and location (e.g., Figs. 1,2). To account for slight ship-course deviations
327 between different legs (Fig. 1b), all of the cloud macroscopic data are binned to a uniform
328 great-circle route with 40-m resolution (the approximate distance covered by the ship in 4
329 s) in order to examine the evolution of cloud properties along this representative great-
330 circle transect. Finally, all the cloud macroscopic data are averaged over 36-km (the
331 approximate distance covered by the ship in 1 hr) and converted to the corresponding
332 latitude along the great-circle route. The frequency of occurrence of MBL cloud every
333 36-km are considered to represent the CF over that area and are referred to as CF_{36} in this
334 paper.

335

336 3.3 Precipitation classification

337

338 KAZR observations, the KAZR-derived hydrometer mask, ceilometer-derived cloud-base
339 heights, surface rainfall occurrence from the weather stations, and 0°C isotherm heights

340 derived from interpolated radiosonde data are used to characterize precipitation. KAZR
341 echoes are classified as either cloud or precipitation; no attempt is made to distinguish ice
342 hydrometeors from liquid cloud drops or precipitation. Because the cloud-base heights
343 are determined from the ceilometer data, every KAZR echo below the first cloud-base
344 height is classified as precipitation. The ceilometer quality control flag was checked to
345 ensure that no water was present on the ceilometer window (which would occur in the
346 case of intense precipitation reaching the surface), since this would strongly attenuate the
347 signal and result in inaccurate readings.

348 Precipitation is classified into five types (Table 2): virga, drizzle, warm rain, cold rain,
349 and deep convective rain (e.g., Fig. 3d). Precipitation that is not detected at the surface is
350 either virga or drizzle. The distinction between the two is based on the detection of
351 KAZR echoes in the lowest range gate (around 120 m ASL before Leg11A, and 240 m
352 ASL for the later legs): virga is defined as precipitation that is detected at least 50 m
353 below the ceilometer cloud base and does not reach the lowest KAZR range gate,
354 whereas drizzle is detected at the KAZR lowest range gate. This distinction provides a
355 qualitative indicator of light rain intensity and indicates the portion of the subcloud layer
356 affected by evaporation. Under this proposed definition only rain that falls through a
357 cloud and not that from the side of a cloud could be considered virga. Precipitation is
358 defined as warm (cold) rain when it is detected at the surface and when the first KAZR-
359 derived cloud top is above 3 km but lower (higher) than the 0°C isotherm height,
360 regardless of the ceilometer-derived cloud-base height. Precipitation is defined as deep
361 convective rain when it is detected at the surface and when the radar reflectivity at the
362 lowest range gate is greater than 0 dBZ and also greater than that at the first KAZR

363 cloud-top height. Similar to the cloud macroscopic data, the precipitation data for each
364 leg are averaged over 36-km along the great-circle route.

365

366 3.4 Radiosonde analysis

367

368 Radiosonde data are used to determine the thermodynamic structure of the lower
369 atmosphere. Emphasis in this study is placed on identifying the inversion and transition
370 layers, which are closely associated with MBL stratification and MBL clouds. The
371 inversion layer is defined as all levels around the maximum increase of temperature with
372 height that occurs between 500 m and 3 km that have an increase of temperature and a
373 decrease in water vapor mixing ratio (r) with height (see Rémillard et al., 2012 for more
374 details).

375 Following the algorithm of Yin and Albrecht (2000), a parameter μ is defined for each
376 level below the inversion base in terms of the potential temperature (θ) and r :

377
$$\mu = -\left(\frac{\partial\theta}{\partial P} - \frac{0.608\theta}{1+0.608r} \frac{\partial r}{\partial P}\right), (1)$$

378 and the transition layer is defined whenever the maximum value of μ is positive and
379 consists of all levels below the base of the inversion at which μ is greater than 1.3 times
380 its mean value over the entire region below the inversion. Examples of the sounding-
381 derived inversion and transition layers under conditions of broken Cu and overcast Sc are
382 illustrated in Figs. 4a and 4b, respectively.

383 The sounding data for each vertical profile are smoothed prior to any analysis using only
384 the next-nearest points to remove small-scale variability and to provide smooth local
385 gradients. To preserve the features of the transition and inversion layers, a layer-by-layer
386 averaging procedure is performed when averaging various profiles together (Augstein et
387 al., 1974; Yin and Albrecht, 2000; Rémillard et al., 2012). Between the surface and 3 km,
388 the profiles are broken into 5 layers: the layer below the transition, the transition layer,
389 the layer between the transition and the inversion, the inversion layer, and the layer above
390 the inversion. Each layer is averaged separately using a normalized height coordinate
391 (from 0 to 1) and is combined with other layers using the averaged base and top heights
392 of the layers as the height coordinate.

393 The difference between equivalent potential temperature at the inversion top ($\theta_{e(\text{inv_top})}$)
394 and base ($\theta_{e(\text{inv_base})}$),

395
$$\Delta\theta_e = \theta_{e(\text{inv_top})} - \theta_{e(\text{inv_base})}, \quad (2)$$

396 provides information on the stability of the MBL: lower values of $\Delta\theta_e$ indicates greater
397 cloud-top entrainment instability because the entrained air, after becoming saturated,
398 would be more negatively buoyant and would continue to sink further (Lilly, 1968;
399 Deardorff, 1980). Additionally, numerical calculations demonstrate that the entrainment
400 rate increases abruptly when $\Delta\theta_e$ decreases below a critical value (Deardorff, 1980).
401 Approximately 10% of the profiles contained an artificial peak in water vapor mixing
402 ratio immediately above Sc due to the wet-bulb effect of the radiosondes; when this
403 occurred, $\theta_{e(\text{inv_top})}$ was replaced by the value of θ_e immediately below this peak.

404 The inversion strength is quantified using the lower-tropospheric stability (LTS; Klein
 405 and Hartmann, 1993) and by the Estimated Inversion Strength (EIS; Wood and
 406 Bretherton, 2006). LTS is defined as the difference between the potential temperature at
 407 700 hPa (θ_{700}) and that at the surface ($\theta_{surface}$),

$$408 \quad LTS = \theta_{700} - \theta_{surface} . \quad (3)$$

409 EIS is defined as

$$410 \quad EIS = LTS - \Gamma_m^{850} (Z_{700} - LCL) , \quad (4)$$

411 where Γ_m^{850} is the moist adiabat at 850 hPa, Z_{700} is the 700 hPa height, and LCL is the
 412 lifting condensation level. The LCL can be approximated by Epsy's formula (Bohren and
 413 Albrecht, 1998) in terms of the surface values of the air temperature (T_s), dew point
 414 temperature (T_d), dry adiabatic lapse rate (Γ_d), and pseudo-adiabatic lapse rate (Γ_s) as

$$415 \quad LCL = \frac{T_s - T_d}{\Gamma_d - \Gamma_s} ; \quad (5)$$

416 numerically, the value of LCL (in m) is approximately 125 times the difference $T_s - T_d$ (in
 417 K). EIS, and previously LTS, have been shown to correlate well with the occurrence of
 418 the Sc-to-Cu transition (Wyant et al., 1997); however, EIS is a more physically based
 419 quantity as it accounts for the influence of the accumulated static stability between the
 420 inversion and the 700-hPa level (Wood and Bretherton, 2006).

421 To derive the statistics, all the sounding data are averaged over 36-km and converted to
 422 corresponding latitude along the great-circle route. As the statistics of the inversion layer
 423 presented below are based primarily on measurements from radiosondes, which were

424 launched four (eight) times every day (see Section 2.2), each sounding profile is assumed
425 to be representative of the atmospheric structure over the 6 h (3 h) time around the
426 sounding. Due to the sparseness of these data, these statistics might not be as robust as
427 those derived from the radar, but nonetheless they are expected to accurately represent
428 the observed trends.

429

430 3.5 Systematic MBL decoupling and Sc breakup detection

431

432

433 The commencement of the systematic MBL decoupling (DE) and Sc breakup (CB)
434 towards Hawaii has been determined for each leg in order to better understand their
435 triggering factors. At each location, the difference in the mean water vapor specific
436 humidity (q_v) between the bottom 25% of the MBL and the top 25% of the MBL is
437 calculated:

$$438 \quad \Delta q = q_v(\text{bot}) - q_v(\text{top}). \quad (6)$$

439 This quantity is related to Δz_b , the difference in the Sc cloud bases formed below the
440 inversion (z_b) and the LCL:

$$441 \quad \Delta z_b = z_b - LCL, \quad (7)$$

442 where z_b is calculated as the maximum MBL cloud bases (averaged over 36 km) within
443 four degrees longitude surrounding each radiosonde. The linear relationship between Δq
444 and Δz_b (Figure 5a) with the slope (276 m kg g^{-1}) and intercept (200 m) comparable to
445 those found in Jones et al. (2011), demonstrate that Δq is a robust proxy for Δz_b . Some

446 scatter is introduced since Δq comes from a single profile while Δz_b is an averaged
447 maximum value. Biases might be introduced when no Sc was detected near a radiosonde
448 or when MBLH was not well represented due to the very shallow MBL near the coast of
449 California. Thus only those radiosondes within 1.5 standard deviations of the least square
450 fit and that to the west of 123°W were used (336 in total). A threshold of $\Delta q > 1.5 \text{ g kg}^{-1}$
451 (or equivalently $\Delta z_i > 600 \text{ m}$) is found appropriate to capture the systematic decoupled
452 MBL (Fig. 5b). Compared to the threshold of $\Delta q > 0.5 \text{ g/kg}$ ($\Delta z_i > 150 \text{ m}$) for all kinds of
453 decoupling in VOCAL-REx (Jones et al., 2011), the systematic decoupling showed much
454 stronger moisture stratification below the inversion. Subsequently, the DE during each
455 transect is then defined as the most easterly profile of a group of profiles with continuous
456 decoupling features ($\Delta q > 1.5 \text{ g kg}^{-1}$). Between the detected and the nearest east radiosonde
457 launches, the Δq criteria for decoupling is replaced by the difference of the instantaneous
458 ceilometer-derived cloud bases height and LCL calculated by the ship-measured T and
459 RH. Compared to the systematic decoupling, the weak decoupled MBL is also studied in
460 this paper and is defined as the MBL with $\Delta z_i > 150 \text{ m}$ (Consistent with Jones et al., 2011).

461

462 Due to mesoscale influences, CF_{36} sometimes shows variability and does not represent
463 well the major cloud evolution along the transect. To reduce the effects of mesoscale
464 variability and to more objectively capture CB, the frequency of occurrence of the MBL
465 clouds was averaged over 108 km (CF_{108}). CB is then defined as the location along the
466 transect from California to Hawaii where CF_{108} decreased from being greater than 80%
467 for at least three continuous points (324 km) east of 130°W to being less than 15%.
468 Values of CF_{MBL} were generally not sensitive to the above criteria. No cloud breakup

469 points are determined if values of CFMBL east of 130°W were not sufficiently high
470 (Leg06A, Leg06B, Leg08A, Leg08B, and Leg17B) or if they did not become sufficiently
471 low (Leg15B). Those legs are associated with either mid-latitude or tropical cyclones, or
472 very strong cloud outbreaks thus not represent the Sc breakup in a general sense, and
473 their exclusion helps to elucidate the more general aspects of the transition.

474

475

476

477 **4. RESULTS**

478

479 The results presented below are separated into two sections. The first section includes
480 general statistical description of MBL clouds, precipitation, thermodynamics and their
481 seasonal behavior. The second section focuses on the study of MBL systematic
482 decoupling and cloud breakup.

483

484 4.1 General statistics of MBL clouds, precipitation and thermodynamics

485 4.1.1 Cloud and Precipitation Occurrence

486 The fraction of time that the four main cloud types defined in Section 3.2 are detected
487 (i.e., their frequencies of occurrence over individual legs) is shown in Figure 6a. MBL
488 clouds are by far the most frequently observed cloud type, and all other types contribute
489 less than 10% to the total observed hydrometeor occurrence in the column. The frequency
490 of occurrence of MBL clouds has a broad maximum near 75% between 125°W and

491 135°W and decreases steadily to values near 20% near Hawaii. Lower values of MBL
492 cloud occurrence are also observed near the coast of California. The frequency of
493 occurrence of precipitation from MBL clouds (Fig. 6b) exhibits a very similar pattern to
494 that of MBL cloud occurrence.

495 A seasonal breakdown of MBL cloud occurrence is shown in Fig. 6c. The frequencies of
496 occurrence of MBL clouds in the warm season and the cold season exhibit generally
497 similar spatial patterns. During the warm season a broad maximum near of 90% between
498 ~122°W and ~132°W is observed, whereas that during the cold season a maximum near
499 of 70% between ~128°W and ~132°W is observed. On average, the observed MBL cloud
500 occurrence in the warm season is 20-40% higher than that observed in the cold season.

501 As expected, the frequency of occurrence of precipitation (Fig. 6d) is also generally
502 higher during the warm season than during the cold season. During the warm season
503 precipitation exhibits a maximum of ~80% between ~123°W and ~131°W, but during the
504 cold season the broad maximum, at ~55% is observed between ~128°W and ~136°W. In
505 contrast to the relatively high frequency of occurrence of clouds during the warm season
506 east of 124°W, the corresponding frequency of occurrence of precipitation decreases
507 rapidly. This might be attributed to the presence of thin clouds at this region (average
508 thickness of 180m east of 124°W compared to 300m west of 124°W).

509 The mean cloud-base height (H_b , Fig. 6e) and mean cloud-top height (H_t , Fig. 5f) of the
510 lowest cloud layer show little seasonal variability except for the regions east of 125°W.
511 Mean values of H_b increase gradually from 0.6 km near the coast of California to 1 km
512 near 135°W and remain at around 1 km further west but exhibit increasing fluctuations,

513 reflecting the intermittent presence of small-scale Cu clouds below the Sc. H_t values are
514 on average 230 m greater than those of H_b and also exhibit fluctuations west of 135°W .
515 East of 125°W we found the most noticeable difference in H_b and H_t between the warm
516 and cloud season. The lower H_b east of 125°W during the warm season might be
517 attributed to the stronger coastal upwelling that results to lower SST (Fig. 6g), while the
518 higher H_t east of 125°W during the cold season might be attributed to a frontal system
519 that occurred during Leg06B and a low-pressure system during Leg07B.

520 Most of the precipitation produced by MBL clouds is in the form of virga (Fig. 6h). Virga
521 is the dominant precipitation type over the entire transect except for the region east of
522 126°W . The virga frequency of occurrence peaks at 40% near 130°W , whereas that of
523 drizzle (precipitation that reaches the surface) exhibits a sharp maximum of more than 30%
524 near 124°W , contributing to the noticeable peak of precipitation frequency at this location
525 (Fig. 6b and Fig. 6d). The increasing frequency of occurrence virga and decreasing
526 frequency of occurrence of drizzle from 124°W to 130°W (Fig. 6h) might be attributed to
527 the increasing cloud-base height (Fig. 6e) caused by the warmer SST (Fig. 6g) away from
528 the California coast. The low frequencies of occurrence (less than 10%) of both virga and
529 drizzle near Hawaii are consistent with the low frequency of occurrence of MBL clouds
530 there (Fig. 6a, 6b, 6c). At the same time, the low frequencies of occurrence of both virga
531 and drizzle east of 124°W is associated with the presence of thinner clouds in that region
532 (Fig. 6e, 6f) and to the higher in-cloud cloud droplet concentrations. The mean surface
533 CCN at 119°N is on averaged $150/\text{cm}^3$ higher than that around 122°W (Lohmann and
534 Feichter, 2005).

535

536 4.1.2 Spatial and seasonal behavior of MBLH and EIS

537 The mean and seasonal values of MBLH and EIS (Eq. 4) along the MAGIC transect are
538 shown in Fig. 7. The mean MBLH (Fig. 7a) generally increases from California to
539 Hawaii, with slightly lower values in the warm season. The largest differences in MBLHs
540 between the warm season and cold season are observed east of 125°W, with those
541 observed during the cold season being nearly twice as high as those during the warm
542 season near the coast of California. The low MBLH east of 125°W during the warm
543 season results in thin clouds (see section 4.1.1) and correspondingly a low frequency of
544 precipitation there (Fig. 6d). The deeper MBL during the cold season is consistent with
545 the high H_t (Fig. 6f), which might be due to synoptic influences (see Section 4.1.1). The
546 decrease in MBLH between 145°W and 150°W can also attributed to synoptic influences
547 and is discussed below. The trend in MBLH along the MAGIC transect (Fig. 7a) follows
548 that of H_t (Fig. 6f) east of 135°W, indicating the capped feature of the MBL, while values
549 of H_t west of 135°W are generally less than those of MBLH, indicating MBL decoupling
550 and Cu-under-Sc cloud regimes.

551 The mean EIS (Fig. 7b) decreases gradually from 9 K near the coast of California to
552 around 2 K near Hawaii, with values in the warm season being 1-3 K higher and those
553 during the cold season 1-3 K lower, the differences decreasing toward Hawaii. EIS shows
554 strong linear relationship with SST along the transect (figure not shown), while in terms
555 of the seasonal variability, leg-mean EIS is mainly determined by the leg-mean potential
556 temperature at 700 hPa (Fig. 7c). This quantity exhibits a larger seasonal variability,
557 ranging from 7 K to 11 K among different legs due to the subsidence of the dry warm air

558 from above the inversion layer, while θ_{surface} , which depends largely on SST, varies less
559 than 1 K between seasons.

560 It is likely that the seasonal variability of EIS (Fig. 7b) contributes to the seasonal
561 variability in the frequency of occurrence of MBL clouds (higher amount of MBL cloud
562 in the warm season and lower in the cold season), consistent with the conclusion of Wood
563 and Bretherton (2006) that stratus cloud fraction is largely determined by EIS. The higher
564 frequency of occurrence of MBL clouds during the warm season when EIS was higher
565 (Fig. 6c) reflects the importance of the strong warm-season large-scale Hadley cell (Xu
566 and Cheng, 2013) that brings dry warm air downward, leading to higher values of θ_{700}
567 (Fig. 7c).

568

569 4.1.3 Sc and Cu occurrence and thermodynamic features

570

571 Frequencies of occurrence of the two important MBL cloud types, Sc and Cu, are
572 examined in this section. Statistics of total and seasonal occurrence of Sc and Cu are
573 shown in Fig. 8. The frequency of occurrence of Sc attains a broad maximum near 60%
574 between 125°W and 135°W, and decreases to near 0% near Hawaii. The decrease in
575 frequency of occurrence of Sc is not uniform along the MAGIC transect, and is greatest
576 near 137°W and near 144°W, consistent with the sharp decreases in MBL cloud
577 occurrence (Fig. 6a) at these locations. In contrast, the frequency of occurrence of Cu is
578 always low, but steadily increases from near 5% near the coast of California to over 10%
579 near Hawaii. Sc are more frequently observed during the warm season than during the
580 cold season, while the occurrence of Cu is almost the same for both seasons, with slightly

581 more frequent cold-season Cu close to the coast of California and slightly more warm-
582 season Cu close to Hawaii.

583 The comparison between ceilometer-detected Sc base height and MBLH from 143
584 corresponding radiosondes indicate that 80% of the Sc clouds formed directly below the
585 MBL inversion. Accordingly ceilometer-detected Cu bases heights show broader
586 distribution but mainly occur near the top of the transition layer detected in 74
587 corresponding radiosondes (figures not shown). Fig. 9 shows the averaged
588 thermodynamic structure for Cu (including multi-layer MBL cloud) and single-layer Sc.
589 A total of 141 radiosonds were analyzed: 104 with Sc near the inversion (Sc top no more
590 than 200 m below the MBLH) and 37 with Cu near the transition or multilayer cases (Cu
591 base more than 200 m above the transition-layer tops). Application of a layer-by-layer
592 averaging method for the soundings for each cloud category (see section 3.4 for details)
593 requires detectable inversion and transition layers. Analyses of the MAGIC sounding data
594 indicate that both layers are present in the vast majority (94%) of the soundings. Note that
595 the presence of a transition layer does not necessarily indicate a systematic decoupled
596 MBL (see section 3.5).

597 As seen in Fig. 9, the large vertical gradients in potential temperature and water vapor
598 mixing ratio near 1.5 km indicate the heights and strengths of the inversion layers, while
599 the smaller changes below 1 km correspond to transition layers (Fig. 9). The standard
600 deviations of both potential temperature and mixing ratio for both categories are
601 relatively small below the inversion layer, indicating little seasonal variability in profiles
602 of these quantities. Sc cases exhibit lower inversion- and transition-layer heights than Cu
603 cases, and they have greater potential temperature differences across the inversion

604 (around 10 K compared to near 5 K for Cu); the mixing ratio differences across the
605 inversion are nearly the same for both cases, around 6 gkg⁻¹. Sc cases exhibit smaller
606 jumps across the transition layer than Cu for both potential temperature (< 0.5 K
607 compared to near 1 K for Cu) and mixing ratio (< 1 gkg⁻¹ compared to 2 gkg⁻¹ for Cu);
608 thus Cu cases are associated with a much stronger transition layer than Sc, implying a
609 greater chance of a decoupled MBL. However, this stronger transition results in part
610 because the cumuli help maintain the transition layer by mixing dry and warm air from
611 the free troposphere downward.

612

613 4.2 MBL systematic decoupling and cloud breakup

614

615 The locations of DE and CB for each leg are shown in Fig. 10. Consistent with previous
616 studies (e.g. Albrecht et al., 1995a; Bretherton and Pincus, 1995; Wyant et al. 1997;
617 Sandu and Stevens, 2011), DE occurred east of CB (when the latter was determined) on
618 all legs. In this section, legs with both DE and CB detected are further examined with the
619 intention to discuss some of the potential controlling factors that are usually neglected in
620 the numerical simulations.

621

622 4.2.1 Possible controlling factors of MBL systematic decoupling

623 Since DEs and CBs occurred at different locations for individual transects, a
624 normalization of each leg is required in order to develop composites of variables across

625 these points. Each leg is divided into three regions: east of DE, between DE and CB, and
626 west of CB, and the distance along the transect in each region is normalized (that is, for
627 each leg, the distance from California to any location east of DE is divided by the
628 distance between California and CB, and the CFMBL values for all legs used are
629 averaged over this normalized distance, and similarly for the region between DE and CB,
630 CB and Hawaii).

631 The radiosonde-derived LCL, shown in Fig. 11a as a function of this normalized distance,
632 increases from 450m to 750m east of DE, decreases slightly to the west of DE, and
633 remains at around 750m to the west of CB. Numerical simulations accurately capture the
634 increasing trend of LCL with increasing SST over the well-mixed MBL (Wyant et al.
635 1997; Sandu and Stevens, 2011). The LCL height is more sensitive to the surface
636 moisture than to the temperature. Thus, the increasing LCL height implies a gradual
637 drying of the MBL, mainly due to the increasing entrainment rate with higher SST that is
638 necessary to maintain the energy balance (Bretherton and Wyant, 1997). During MAGIC,
639 it is found that the LCL increase rapidly near DE (Fig. 11a), and the maximum increase
640 in LCL with SST near DEs range from 122m/K to 369m/K. The MAGIC observations
641 suggest that this sudden dryness of the MBL is correlated with the entrainment of dryness
642 above the inversion.

643 Fig. 11b shows the mean $\Delta\theta_e$ (i.e., averaged over legs) over normalized distance from
644 California to DE. $\Delta\theta_e$ initially increased to near -2 K and then decreased to -6 K at DE.
645 This decrease is mainly due to the large mean mixing ratio difference across the inversion
646 (Fig. 11c). Plausible explanations for the drier conditions above the inversion are small
647 displacements of the Hadley cell or cold outbreaks behind trailing cold fronts of mid-

648 latitude cyclones indicated by the increasing sea surface pressure from California to DE
649 (Fig. 10b). The advection due to the large-scale circulation might also contribute.
650 Meanwhile, the increase in both the potential temperature above the inversion (caused by
651 the subsidence of the dry warm air) and that below (due to the increasing SST; Fig. 6g)
652 explains the maintenance of the mean potential temperature difference across the
653 inversion of near 6 K (Fig. 11d), which contributed less to the decrease $\Delta\theta_e$. The drop in
654 $\Delta\theta_e$ east of the DE point increase (Fig. 12) the cloud top entrainment instability and the
655 entrainment rate (Deardorff, 1980) and subsequently less moisture in the MBL.
656 Consistent with the ‘deepening-warming mechanism’ (Bretherton and Wyant, 1997), our
657 analysis concurs that entrainment plays a crucial role in inducing the MBL decoupling
658 and the MAGIC observations also suggest that the dry warm air above the inversion
659 might be an important trigger.

660 One would expect a dramatic increase of the LHF east of DE due to the dryness of the
661 MBL; however, the mean surface latent heat maintained around 120 W/m^2 during that
662 period (Fig. 12a). Therefore, the role of increasing latent heat fluxes in generating the
663 systematic decoupling as suggested in the idealized model (Bretherton and Wyant, 1997)
664 is not captured by the MAGIC observations. The reduction of the mean surface wind
665 speed from California to DE (Fig. 12b) regulate the increase of the LHF, when the ship
666 moved from the edge to the center of the high-pressure system (Fig. 10b). Thus, we
667 conclude that LHF might be important in maintaining the systematic decoupling, but LHF
668 does not play the dominant role in inducing decoupling in MAGIC, which is consistent
669 with the conclusion of Jones et al (2011).

670 Apart from the systematic decoupling, the weak decoupling ($\Delta z_i > 150\text{m}$) east of DE are
671 also investigated. Broad peaks of the frequency of occurrence of virga and drizzle were
672 found east of DE, while these frequencies decreased to below 20% when MBL was
673 decoupled (figures not shown). We found 87% of which are associated with precipitation.
674 We conclude that precipitation might play a role in inducing decoupling, but this
675 decoupling is usually weak and not continuous, thus precipitation did not show a
676 dominant impact on systematic decoupling. Meanwhile, the diurnal decoupling might
677 also partly explain the weak decoupling east of DE since 73% of which occurred in the
678 local daytime from 6:00 am to 6:00pm.

679

680 4.2.3 Possible controlling factors of MBL cloud breakup during MAGIC

681 Values of CF_{36} are typically high along the eastern part of the MAGIC transect (Fig. 10a),
682 especially during the warm season (Fig. 6). The locations where CF_{108} drop to below 50%
683 are usually close to CB (CF_{108} drops to below 15%), indicating the abrupt MBL cloud
684 breakup (Fig. 10a) At the same time, CB is typically located on the west edge of high-
685 pressure systems (Fig. 10b), implying the role of synoptic interference in the observed
686 MBL cloud breakup.

687 To further investigate this, we analyze the MBL wind profiles near the CB points. A clear
688 synoptic-induced divergence pattern is found. Fig. 13a shows median profiles of zonal
689 (ΔU) and latitudinal (ΔV) wind difference of the composed U(V) wind east and west of
690 CB in the small and large region. This small region is bounded by two days of radiosonds
691 (~ 1600 km) surrounding CB while the large region refers to the whole transect. The

692 profiles shown in Fig. 13a show little sensitivity to the details of the region selected to
693 estimate the wind differences. The well-separated zonal and latitudinal wind differences
694 around the CB indicate a systematic divergence in the MBL since the wind to the west of
695 CB is more easterly ($\Delta U < 0 \text{ m/s}$), and more southerly ($\Delta V > 0 \text{ m/s}$) than that to the east. We
696 interpret the east of CB wind pattern as the stable high-pressure systems and the west of
697 CB wind pattern as the signature of approaching mid-latitude cyclone systems. Strong
698 uplifting convergence in the east-approaching cyclones was compensated by the
699 divergence nearby. The drop of the MBLH near CBs provides evidence of the
700 compensating subsidence (Fig. 13b), which is absent in the idealized model with
701 uniformed large scale forcing. Moreover, the averaged mixing ratio difference above the
702 inversion was nearly doubled in the small region (figures not shown). We conclude that
703 the switch of the synoptic environment to the unstable cyclone system can fast break up
704 the MBL cloud and drive vigorous Cu or deep convective clouds.

705

706 **5. SUMMARY AND DISCUSSION**

707

708 The MAGIC field campaign, with nearly 200 days of ship-based observations during 20
709 round trips along the 4000 km transect between California and Hawaii, provided an
710 unparalleled opportunity to acquire data on properties of MBL clouds, precipitation and
711 thermodynamic structure. The measurements obtained during that campaign are used in
712 this manuscript to examine the location and potential controlling factors of systematic
713 MBL decoupling and Sc breakup.

714 MBL clouds were by far the most frequently observed cloud type during the MAGIC
715 campaign. MBL clouds occurred more often during the warm season (Fig. 5), reflecting
716 the importance of the strong warm-season large-scale Hadley cell (Xu and Cheng, 2013).
717 Among the different MBL cloud types, Sc was the dominant MBL cloud type and
718 occurred more frequently during the warm season than during the cold season (Fig. 8b),
719 while the occurrence of Cu was less strongly affected by subsidence and exhibited nearly
720 the same behavior for both seasons (Fig. 8b).

721

722 The formation of Sc just below the inversion requires a shallow MBL with a strong
723 inversion and a weak transition (Fig. 9), providing a greater opportunity to have well-
724 mixed MBL conditions. In contrast, Cu and multi-layer clouds are usually associated with
725 a much stronger transition, implying a greater chance of decoupling in the MBL.

726 There was a high frequency of occurrence of precipitation throughout the campaign.
727 However, the precipitation from the MBL clouds is weak and often evaporated well
728 before reaching the ocean surface (Fig. 6e). EIS experienced a seasonal variation caused
729 by that of θ_{700} (Fig. 7c), and generally decreased due to the increasing SST. MBLH
730 generally increased along the transect from California to Hawaii (Fig. 7). East of 135°W
731 the spatial behavior of MBLH parallels that of the first cloud-top height (Figs. 5f and 6d),
732 indicating the capped feature of the MBL.

733 The locations of MBL systematic decoupling are determined for individual legs. It is
734 found that a threshold of $\Delta q > 1.5$ g/kg separates the well-mixed profiles from the
735 systematic decoupled ones (Fig. 5b). Compared to the threshold of $\Delta q > 0.5$ g/kg⁻¹ found in
736 VOCAL-REx (Jones et al., 2011), the MAGIC systematic decoupling showed much

737 stronger moisture stratification below the inversion. Precipitation and solar radiation
738 correlate well with the weak decoupling points between California and DEs, but neither
739 of them plays a dominant role in the systematic decoupling.

740 A rapid increase of LCL height was found near DEs (Fig. 11s), indicating more rapid
741 drying of the MBL. Correspondingly, the mean cloud top instability showed a sudden
742 increase mainly due to the large mixing ratio difference across the inversion (Fig. 11b,c).
743 These observations imply that the dry warm air from above the inversion is likely of great
744 importance to trigger the systematic decoupling. Consistent with the results in VOCAL-
745 REx (Jones et al., 2011), LHF does not play the dominant role in inducing systematic
746 decoupling in MAGIC. Meanwhile, the mixed layer cloud thickness during MAGIC did
747 not correlate well with the systematic decoupling due to the sudden change of LCL near
748 DEs, further implying that the strong entrainment was driven more by the cloud top
749 instability than by the in-cloud turbulence.

750 DEs nearly always occurred east of CBs (if present) (Fig. 10). MBL clouds tend to
751 breakup abruptly at a location that is typically on the west edge of high-pressure systems
752 (Fig. 10b). A change in synoptic pattern (i.e. different air mass) was often found near CB,
753 which is associated with systematic divergence in the MBL. The divergence, together
754 with downdrafts, compensated for the convergent uplifting in the approaching cyclones.
755 We conclude that the cloud evolution in the idealized model seldom occurs in reality due
756 to synoptic interference.

757

758 **6. ACKNOWLEDGMENTS**

759

760 The MAGIC deployment was supported and undertaken by the U.S. Department of
761 Energy (DOE) Atmospheric Radiation Measurement (ARM) Program Climate Research
762 Facility. The current research was supported by the DOE Atmospheric System Research
763 (ASR) Program (Office of Science, OBER). ERL was supported by the ASR Program
764 under Contract No. DE-AC02-98CH10886. Data used for the analyses were downloaded
765 from the ARM archive (www.arm.gov) except for the MARMET and MARFLUX data,
766 which were provided by Dr. Michael Reynolds of RMR Co. We thank David Painemal of
767 NASA Langley Research Center for providing surface cloud condensation nuclei (CCN)
768 data. We acknowledge the team of scientists and technicians who made this work
769 possible by collecting the data and maintaining the instruments, and especially Horizon
770 Lines and the Captain and crew of the Horizon *Spirit* for their hospitality. Special thanks
771 go to the cloud research group at McGill University (www.clouds.mcgill.ca) for their
772 helpful comments and constructive criticism.

773

774

775

776

777

778

779

780

781 **Appendix:**

782 Table A1 about here.

783

784 B. MAGIC Instrument Status

785 **Instrument Status Table Leg03A to Leg09B**

786 The first leg with MAGIC instrumentation was Leg01B during which the ISAR
787 was installed. During Leg02A and Leg02B, for which instrument status designations are
788 not listed, the radars and other instruments were being set up; some collected data during
789 these legs. During Leg03 most of the instruments were up and collecting data. On
790 Leg09B, the instruments were without power for extended times and were being shut
791 down. The instruments were removed from the ship after Leg09B from January, 2013
792 until May, 2013.

793 Fig. 14 about here.

794 **Instrument Status Table Leg10A to Leg18B**

795

796 MAGIC instruments were redeployed during Leg10A, and the campaign
797 continued until the end of Leg20B. The technicians did not report instrument status
798 designations for Leg19A and Leg19B, but these were probably similar to those for
799 Leg18B. During Leg20A and Leg20B the instruments were being turned off, so few data
800 were collected during these legs (although sonde launches occurred on Leg20A,

801 meteorological data were collected until the ship returned to port, and both radars were
802 operating for most of the two legs).

803 Fig 15 about here.

804

805 Table A2 about here.

806

807

REFERENCES

808 Albrecht, B. A., 1984. "A model study of downstream variations of the thermodynamic
809 structure of the trade winds." *Tellus*, **36A**, 187-202.

810

811 Albrecht, B. A., Randall, D. A., & Nicholls, S. (1988)."Observations of marine
812 stratocumulus clouds during FIRE." *Bulletin of the American Meteorological Society*,
813 **69**(6), 618-626.

814

815 Albrecht, B. A., C. S. Bretherton, D. Johnson, W. H. Scubert and A. S. Frisch (1995a).
816 "The Atlantic stratocumulus transition experiment-ASTEX." *Bulletin of the American*
817 *Meteorological Society* **76**(6): 889-904.

818

819 Albrecht, B. A., Jensen, M. P., & Syrett, W. J. (1995b). "Marine boundary layer structure
820 and fractional cloudiness." *Journal of Geophysical Research: Atmospheres* (1984–2012),
821 **100**(D7), 14209-14222.

822

823 Augstein, E., H. Schmidt and F. Ostapoff (1974). "The vertical structure of the
824 atmospheric planetary boundary layer in undisturbed trade winds over the Atlantic
825 Ocean." *Boundary-Layer Meteorology* **6**(1-2): 129-150.

826

827 Bohren, C. and B. Albrecht (1998). *Atmospheric Thermodynamics*, Oxford University
828 Press, New York, USA.

829

830 Boutle, I., R. Beare, S. E. Belcher, A. Brown and R. S. Plant (2010). "The moist
831 boundary layer under a mid-latitude weather system." *Boundary-layer meteorology*
832

833 Bretherton, C. S., & Pincus, R. (1995). "Cloudiness and marine boundary layer dynamics
834 in the ASTEX Lagrangian experiments. Part I: Synoptic setting and vertical structure. "
835 *Journal of the atmospheric sciences*, 52(16), 2707-2723.
836

837 Bretherton, C. S. and M. C. Wyant (1997). "Moisture transport, lower-tropospheric
838 stability, and decoupling of cloud-topped boundary layers." *Journal of the Atmospheric*
839 *Sciences* **54**(1): 148-167.
840

841 Cadeddu, M. (2012). *Microwave Radiometer-3 Channel (MWR3C) Handbook*, DOE
842 *Office of Science Atmospheric Radiation Measurement (ARM) Program (United States)*.
843

844 Cheng, A. and K.-M. Xu (2013). "Evaluating Low Cloud Simulation from an Upgraded
845 Multiscale Modeling Framework Model. Part III: Tropical and Subtropical Cloud
846 Transitions over the Northern Pacific." *Journal of Climate* **26**: 5761-5781.
847

848 Deardorff, J. (1980). "Cloud top entrainment instability." *Journal of the Atmospheric*
849 *Sciences* 37(1): 131-147.
850

851 Fairall, C. W., E. F. Bradley, D. P. Rogers, J. B. Edson, and G. S. Young (1996). "Bulk
852 parameterization of air-sea fluxes for Tropical Ocean-Global Atmosphere Couple-Ocean

853 Atmosphere Response Experiment." *Journal of Geophysical Research* 101 (C2):3747-
854 3764.

855

856 Heck, P. W., B. J. Byars, D. F. Young, P. Minnis, and E. F. Harrison 1990. "A
857 climatology of satellite derived cloud properties over marine stratocumulus regions. "
858 Preprints, Conf. on Cloud Physics, San Francisco, CA, Amer. Meteor. Soc., J1–J7.

859

860 Hildebrand, P. H. and R. Sekhon (1974). "Objective determination of the noise level in
861 Doppler spectra." *Journal of Applied Meteorology* 13(7): 808-811.

862

863 Jones, C. R., Bretherton, C. S., & Leon, D. (2011). "Coupled vs. decoupled boundary
864 layers in VOCALS-REx." *Atmospheric Chemistry and Physics*, 11(14), 7143-7153.

865

866 Karlsson, J., Svensson, G., Cardoso, S., Teixeira, J., & Paradise, S. (2010). "Subtropical
867 cloud-regime transitions: Boundary layer depth and cloud-top height evolution in models
868 and observations." *Journal of Applied Meteorology and Climatology*, 49(9), 1845-1858.

869

870 King, M. D., Y. J. Kaufman, W. Menzel and D. Tanre (1992). "Remote sensing of cloud,
871 aerosol, and water vapor properties from the Moderate Resolution Imaging Spectrometer
872 (MODIS)." *IEEE Transactions on Geoscience and Remote Sensing* 30(1): 2-27.

873

874 Klein, S. A. and D. L. Hartmann (1993). "The seasonal cycle of low stratiform clouds."
875 *Journal of Climate* 6(8): 1587-1606.

876

877 Kollias, P., E. Clothiaux, M. Miller, B. Albrecht, G. Stephens and T. Ackerman (2007).
878 "Millimeter-wavelength radars: New frontier in atmospheric cloud and precipitation
879 research." *Bulletin of the American Meteorological Society* **88**(10): 1608-1624.

880

881 Krueger, S. K., McLean, G. T., & Fu, Q. (1995). "Numerical simulation of the stratus-to-
882 cumulus transition in the subtropical marine boundary layer. Part I: Boundary-layer
883 structure. *Journal of the atmospheric sciences*. " **52**(16), 2839-2850.

884

885 Larson, K., D. L. Hartmann and S. A. Klein (1999). "The role of clouds, water vapor,
886 circulation, and boundary layer structure in the sensitivity of the tropical climate." *Journal*
887 *of Climate* **12**(8): 2359-2374.

888

889 Lewis, E. R., W. J. Wiscombe, B. A. Albrecht, G. L. Bland, C. N. Flagg, S. A. Klein, P.
890 Kollias, G. Mace, R. Reynolds and S. Schwartz (2012). "MAGIC: Marine ARM GPCI
891 Investigation of Clouds."

892

893 Liljegren, J. (1994). Two-channel microwave radiometer for observations of total column
894 precipitable water vapor and cloud liquid water path. *Fifth Symposium on Global Change*
895 *Studies*.

896

897 Lilly, D. K. (1968). "Models of cloud-topped mixed layers under a strong inversion."
898 *Quarterly Journal of the Royal Meteorological Society* **94**(401): 292-309.

899

900 Lohmann, U. and J. Feichter (2005). "Global indirect aerosol effects: a review."
901 Atmospheric Chemistry and Physics **5**(3): 715-737.

902

903 Ma, C.-C., C. R. Mechoso, A. W. Robertson and A. Arakawa (1996). "Peruvian stratus
904 clouds and the tropical Pacific circulation: A coupled ocean-atmosphere GCM study."
905 Journal of Climate **9**(7): 1635-1645.

906

907 Matrosov, S. Y. (2007). "Potential for attenuation-based estimations of rainfall rate from
908 CloudSat." Geophysical Research Letters **34**(5): L05817.

909

910 Miller, M. A., M. P. Jensen and E. E. Clothiaux (1998). "Diurnal cloud and
911 thermodynamic variations in the stratocumulus transition regime: A case study using in
912 situ and remote sensors." Journal of the Atmospheric Sciences **55**(13): 2294-2310.

913

914 Morris, V. (2006). "Microwave radiometer (MWR) handbook." ARM-TR016.

915

916 Neiburger, M. (1961). Studies of the structure of the atmosphere over the eastern Pacific
917 ocean in summer, University of California Press.

918

919 Norris, J. R. and C. B. Leovy (1994). "Interannual variability in stratiform cloudiness and
920 sea surface temperature." Journal of Climate **7**(12): 1915-1925.

921

922 Philander, S., D. Gu, G. Lambert, T. Li, D. Halpern, N. Lau and R. Pacanowski (1996).
923 "Why the ITCZ is mostly north of the equator." *Journal of Climate* **9**(12): 2958-2972.
924

925 Rémillard, J., P. Kollias, E. Luke and R. Wood (2012). "Marine Boundary Layer Cloud
926 Observations in the Azores." *Journal of Climate* **25**(21): 7381-7398.
927

928 Riehl, H., T. Yeh, J. Malkus and N. La Seur (1951). "The north-east trade of the Pacific
929 Ocean." *Quarterly Journal of the Royal Meteorological Society* **77**(334): 598-626.
930

931 Rossow, W. B. and R. A. Schiffer (1999). "Advances in understanding clouds from
932 ISCCP." *Bulletin of the American Meteorological Society* **80**(11): 2261-2287.
933

934 Sandu, I. and B. Stevens (2011). "On the factors modulating the stratocumulus to
935 cumulus transitions." *Journal of the Atmospheric Sciences* **68**(9): 1865-1881.
936

937 Stephens, G. L. (2005). "Cloud feedbacks in the climate system: A critical review."
938 *Journal of Climate* **18**(2): 237-273.
939

940 Teixeira, J., S. Cardoso, M. Bonazzola, J. Cole, A. DelGenio, C. DeMott, C. Franklin, C.
941 Hannay, C. Jakob, Y. Hiao, J. Karlsson, H. Kitagawa, M. Köhler, A. Kuwano-Hoshida, C.
942 LeDrain, A. Lock, M. H. Miller, P. Marquet, J. Martins, C. R. Mechoso, E. V. Meijgaard,
943 I. Meinke, A. M. A. Miranda, D. Mironov, R. Neggers, H. L. Pan, D. A. Randall, P. J.
944 Rasch, B. Rockel, W. B. Rossow, B. Ritter, A. P. Siebesma, P. Soares, F. J. Turk, P. A.

945 Vaillancourt, A. Von Engeln, and M. Zhao (2011). "Tropical and subtropical cloud
946 transitions in weather and climate prediction models: The GCSS/WGNE Pacific Cross-
947 Section Intercomparison (GPCI)." *Journal of Climate* **24**(20): 5223-5256.

948

949 Tiedtke, M., W. A. Hackley and J. Slingo, 1988. "Tropical forecasting at ecmwf: The
950 influence of physical parameterization on the mean structure of forecasts and analyses."
951 *Q. J. R. Meteorol. Soc.*, 114, 639–664.

952

953 Wang, S., B. A. Albrecht, and P. Minnis, 1993. "A regional simulation of marine
954 boundary layer clouds." *J. Atmos. Sci.*, **50**, 4022–4043.

955

956 Wyant, M. C., C. S. Bretherton, H. A. Rand, and D. E. Stevens, 1997. "Numerical
957 simulations and a conceptual model of the subtropical marine stratocumulus to trade
958 cumulus transition." *J. Atmos. Sci.*, **54**, 168–192.

959

960 Widener, K., N. Bharadwaj and K. Johnson (2012). "Ka-Band ARM Zenith Radar
961 (KAZR) Instrument Handbook." DOE Office of Science Atmospheric Radiation
962 Measurement (ARM) Program (United States).

963

964 Wood, R. (2012). "Stratocumulus clouds." *Monthly Weather Review* **140**(8): 2373-2423.

965

966 Wood, R. and C. S. Bretherton (2004). "Boundary layer depth, entrainment, and
967 decoupling in the cloud-capped subtropical and tropical marine boundary layer." *Journal*
968 *of Climate* **17**(18): 3576-3588.

969

970 Wood, R. and C. S. Bretherton (2006). "On the relationship between stratiform low cloud
971 cover and lower-tropospheric stability." *Journal of Climate* **19**(24): 6425-6432.

972

973 Wood, R., C. Mechoso, C. Bretherton, R. Weller, B. Huebert, F. Straneo, B. Albrecht, H.
974 Coe, G. Allen and G. Vaughan (2011). "The vamos ocean-cloud-atmosphere-land study
975 regional experiment (VOCALS-REx): Goals, platforms, and field operations."
976 *Atmospheric Chemistry and Physics* **11**(2): 627-654.

977

978 Xu, K.-M. and A. Cheng (2013). "Evaluating Low Cloud Simulation from an Upgraded
979 Multiscale Modeling Framework Model. Part II: Seasonal Variations over the Eastern
980 Pacific." *Journal of Climate* **26**: 5717-5740.

981

982 Yin, B. and B. A. Albrecht (2000). "Spatial variability of atmospheric boundary layer
983 structure over the eastern equatorial Pacific." *Journal of Climate* **13**(9): 1574-1592.

984

985

986

987

988

7. TABLES

989

990

991 Table 1. Cloud types and characteristics used to differentiate them in the identification

992 algorithm (Ind: indeterminate).

		Type					
		High-level	Mid-level	MBL			Cu congestus and deep convective
				Sc	Cu	Ind	
Minimum cloud base		≥ 6 km	3-6 km	< 3 km*	< 3 km*	< 3 km*	< 3 km
Maximum cloud top		—	—	< 3 km	< 3 km	< 3 km	≥ 3 km
Duration		—	—	≥ 20 min	< 20 min	≥ 20 min	—
Cloud top height standard deviation	[20 min, 2 h]	—	—	< 100 m	—	≥ 100 m	—
	(2 h, 10h]	—	—	< 160 m	—	≥ 160 m	—
	> 10 h	—	—	< 200 m	—	≥ 200 m	—

993

994

995 * Minimum cloud base for MBL clouds are either below 3 km or undetermined

996

997

998

999

1000

1001

1002

1003 Table 2. List of liquid precipitation types and their main characteristics used to
 1004 differentiate them.

1005

1006

	Type				
	Virga	Drizzle	Warm Rain	Cold Rain	Convective Rain
Echo base	> First gate	= First gate	= First gate	= First gate	= First gate
Base reflectivity	—	<0 dBZ	>0 dBZ	>0 dBZ	>0 dBZ & > First Top reflectivity
Surface Rain	No	No	Yes	Yes	Yes
First cloud top height	Below 0°C isotherm	Below 0°C isotherm	Below 0°C isotherm	Above 0°C isotherm	—
Echo below cloud base	Yes (50 m lower)	Yes (50 m lower)	Possible	Possible	Possible

1007

1008

1009

1010

1011

1012

1013

1014

1015 Table A1. Departure and arrival times of each leg.

1016 **All times are UTC.**

1017

	A		B	
	Depart LA	Arrive HI	Depart HI	Arrive LA
Leg00	2012-02-11, 13:30	2012-02-16, 09:00	2012-02-17, 09:00	2012-02-23, 15:00
Leg01			2012-09-14, 23:20	2012-09-20, 13:40
Leg02	2012-09-22, 12:15	2012-09-27, 05:50	2012-09-28, 09:50	2012-10-04, 14:20
Leg03	2012-10-06, 11:30	2012-10-11, 06:30	2012-10-12, 08:00	2012-10-18, 13:30
Leg04	2012-10-20, 11:25	2012-10-25, 06:15	2012-10-26, 06:40	2012-11-01, 13:20
Leg05	2012-11-03, 17:50	2012-11-08, 15:00	2012-11-09, 17:30	2012-11-15, 15:00
Leg06	2012-11-17, 12:20	2012-11-22, 07:30	2012-11-24, 10:15	2012-11-30, 01:20
Leg07	2012-12-01, 13:30	2012-12-06, 09:00	2012-12-07, 08:20	2012-12-13, 14:45
Leg08	2012-12-15, 13:00	2012-12-20, 08:30	2012-12-22, 08:15	2012-12-28, 00:00
Leg09	2012-12-29, 12:30	2013-01-03, 07:00	2013-01-05, 04:50	2013-01-13, 03:35 SEE NOTE 1
Leg10	2013-05-11, 11:20	2013-05-16, 06:20	2013-05-17, 16:30	2013-05-23, 14:00
Leg11	2013-05-25, 11:25	2013-05-30, 06:30	2013-05-31, 11:15	2013-06-06, 13:30
Leg12	2013-06-08, 11:25	2013-06-13, 06:35	2013-06-14, 16:35	2013-06-20, 13:35
Leg13	2013-06-22, 11:30	2013-06-27, 07:45	2013-06-28, 17:30	2013-07-03, 23:10
Leg14	2013-07-07, 17:35	2013-07-12, 06:50	2013-07-13, 11:45	2013-07-18, 23:15
Leg15	2013-07-20, 12:00	2013-07-25, 05:45	2013-07-26, 13:10	2013-08-01, 13:30
Leg16	2013-08-03, 13:30	2013-08-08, 05:40	2013-08-09, 10:15	2013-08-15, 14:30
Leg17	2013-08-17, 18:30	2013-08-22, 10:15	2013-08-23, 17:15	2013-08-29, 13:20
Leg18	2013-08-31, 11:45	2013-09-05, 06:35	2013-09-06, 12:00	2013-09-12, 13:40
Leg19	2013-09-14, 12:25	2013-09-19, 06:20	2013-09-20, 11:20	2103-09-26, 13:55
Leg20	2013-09-28, 11:35	2013-10-03, 06:35	2013-10-04, 10:05	2013-10-10, 13:35 SEE NOTE 2

1018

1019 NOTE 1: During Leg09B the *Spirit* had its engines off for approximately 14 hours on
 1020 2013-01-06 and 2013-01-07; thus the trajectory will look abnormal for this time as the
 1021 ship was drifting. Soon thereafter the entire ship, including the AMF2, was without
 1022 power for approximately one hour, and some instruments might not have resumed
 1023 operation before the end of the leg. Data acquisition stopped 2013-01-11 for some
 1024 instruments and on 2013-01-12 for all instruments. After the *Spirit* arrived in port in Los

1025 Angeles after Leg09B, the AMF2 was removed from the ship (it was completely off the
1026 Spirit by 2013-01-13, 21:00 UTC) and placed in storage, where it remained until
1027 reinstallation on 2013-05-09.

1028 NOTE 2: MAGIC instrumentation was being turned off and packed during Leg20 and all
1029 MAGIC instrumentation was removed from the *Spirit* on 2013-10-10 by 22:00.

1030

1031

1032

1033

1034

1035

1036

1037

1038

1039

1040

1041

1042 Table A2. Statistics (means and standard deviations) of MBL clouds macroscopic
 1043 characteristics. The 1st cloud base, top and thickness in the table refer to those of the
 1044 lowest clouds.

Distance from California Coast		100 km	500 km	1000 km	2000 km	3000 km	3600 km	4000 km
Cloud fractional coverage	Total	0.62±0.44	0.69±0.43	0.74±0.41	0.62±0.38	0.30±0.38	0.33±0.28	0.22±0.28
	Cold	0.49±0.47	0.54±0.46	0.71±0.44	0.54±0.44	0.21±0.27	0.29±0.26	0.17±0.27
	Warm	0.76±0.37	0.88±0.31	0.79±0.40	0.71±0.29	0.40±0.48	0.38±0.31	0.27±0.29
1 st Cloud base [km]	Total	0.51±0.42	0.62±0.34	0.98±0.38	1.14±0.28	1.05±0.40	1.20±0.43	1.11±0.46
	Cold	0.85±0.49	0.69±0.47	1.04±0.52	1.10±0.20	1.09±0.49	1.09±0.46	1.17±0.53
	Warm	0.27±0.08	0.55±0.15	0.92±0.17	1.18±0.36	1.00±0.26	1.32±0.39	1.04±0.37
1 st Cloud top [km]	Total	0.89±0.75	0.91±0.42	1.19±0.28	1.39±0.28	1.20±0.47	1.43±0.47	1.24±0.35
	Cold	1.36±0.90	1.02±0.56	1.17±0.35	1.39±0.24	1.19±0.57	1.31±0.52	1.15±0.31
	Warm	0.48±0.13	0.80±0.16	1.20±0.19	1.39±0.33	1.23±0.34	1.57±0.39	1.33±0.39
1 st Cloud thickness [km]	Total	0.35±0.39	0.27±0.22	0.23±0.15	0.23±0.16	0.19±0.15	0.17±0.13	0.24±0.18
	Cold	0.60±0.51	0.30±0.30	0.18±0.11	0.25±0.16	0.18±0.16	0.15±0.15	0.26±0.19
	Warm	0.18±0.14	0.24±0.11	0.27±0.17	0.21±0.16	0.21±0.15	0.21±0.08	0.21±0.17

1045
 1046 Means and standard deviations of the cloud macroscopic properties at different
 1047 locations along the MAGIC transect (100, 500, 1000, 2000, 3000, 3600 and 4000 km
 1048 from the coast of California) for all applicable MAGIC legs (Leg3-8, Leg11, Leg14-
 1049 17). Data during each leg are binned to a uniform great circle route with 36-km
 1050 resolution.

1051
 1052

1053
1054
1055
1056
1057
1058
1059
1060
1061
1062
1063
1064
1065
1066
1067
1068
1069
1070
1071
1072
1073
1074

Figure Caption List:

1. (a) Horizon *Spirit* showing location of the bridge region where the AMF2 was located, and (b) Tracks of MAGIC legs between California and Hawaii (red lines) and great circle route (blue line).

2. KAZR reflectivity observations for Leg04A (top panel) and Leg04B (bottom panel) with the first ceilometer cloud base shown as black dots. The *Spirit* departed from California on Oct. 21 (2012) and arrived in Hawaii on Oct. 25, then left on Oct. 26 and returned to California on Nov. 1. Graphs are shown with Los Angeles to the right and Honolulu to the left. The ceilometer data for 00:00 to ~21:16 UTC on Oct. 22, 2012 are not available.

3. (a) Cloud classifications for Leg04 with the first ceilometer cloud base shown as black dots. The corresponding KAZR reflectivities can be seen in Fig 2. (b) KAZR reflectivities with the first and second ceilometer cloud base shown as black and red dots respectively for a short time segment on Oct. 21, 2012 during Leg04A. (c) MBL cloud classifications with the first and second ceilometer cloud base shown as black and red dots for the same time period as that shown in Fig. 3b during Leg04A. (d) KAZR reflectivities with the first ceilometer cloud base shown as black dots for a short time period on Oct. 28, 2012 during Leg04B. The pink, light blue and purple backgrounds indicate the occurrence of virga, MBL drizzle, and heavy MBL drizzle, respectively; the yellow background indicates no precipitation during that time period.

1075 4. Profiles of temperature (T), potential temperature (θ), and mixing ratio (r)
1076 from soundings. Green and blue dashed lines show the inversion tops and
1077 bases, while black and red dashed lines show the transition tops and bases. (a)
1078 Sounding launched at 18:08 UTC, October 26, 2012, with broken Cu
1079 overhead. (b) Sounding launched at 12:00 UTC, October 29, 2012, with
1080 overcast Sc overhead.

1081

1082

1083 5. (a) The scatter plot of radiosonde-derived Δq for all the legs and maximum
1084 Δz_b within four degrees longitude surrounding each radiosonde. The solid
1085 black line is the least square fit with slope 276 m kg g⁻¹ and intercept 200m.
1086 The dashed black line represents the thermodynamic argument derived in Jone
1087 et al 2011. The red dots indicate outliers outside 1.5 standard deviation of the
1088 least-square fit. (b) Radiosonde-derived Δq for all the legs along the
1089 normalized path from California to DE to Hawaii.

1090

1091 6. Frequencies of occurrence along the MAGIC transect of (a) the four main
1092 cloud types, (b) MBL clouds and observed MBL-cloud liquid precipitation,
1093 and (c) MBL clouds and (d) observed MBL-cloud liquid precipitation during
1094 the warm and cold season during the warm season (Leg11, Leg14-Leg17:
1095 May 25 -June 6, 2013, July 7-Aug. 29, 2013) and during the cold season
1096 (Leg03-Leg08: Oct. 6-Dec. 27, 2012). Total and seasonal mean along the
1097 MAGIC transect of (e) first cloud base heights, (f) first cloud top heights, and

1098 (g) SSST. The black line shows the total mean, the blue and the red line shows
1099 the mean for cold and warm season respectively. The gray shaded region
1100 indicates one standard deviation of the mean. Frequencies of occurrence along
1101 the MAGIC transect of (h) liquid precipitation types.

1102

1103 7. Total and seasonal mean of (a) MBLH, and (b) EIS along the MAGIC transect.
1104 The gray shaded region indicates one standard deviation of total. The black
1105 line shows the total mean, the blue line shows the mean of the cold season,
1106 and the red line the mean for the warm season, and (c) Leg-mean values of
1107 EIS, SSST, potential temperature at 700 hPa, and potential temperature at the
1108 surface.

1109

1110 8. Frequencies of occurrence of cloud types (a) over the entire deployment and
1111 (b) during the cold season and warm season.

1112

1113 9. Profiles of means and standard deviations of (a) potential temperature and (b)
1114 water vapor mixing ratio composed over the cases with single stratocumulus
1115 at the inversion level (blue dotted line), and single cumulus at the transition
1116 level together with multiple MBL clouds (red solid line), both of which must
1117 contain a transition layer.

1118

1119 10. (a) CF_{36} , (b) the sea surface pressure along the MAGIC transect for individual
1120 legs. The black triangle and the black dots indicate the cloud breakup points

1121 (CB) and the starting points of the MBL systematic decoupling (DE). The red
1122 crosses in (a) indicate the location when CF_{108} drops to below 50% before CB.
1123 White spaces in (a) denote times when CF_{36} was less than 10%, and those in
1124 (b) denote missing data.

1125

1126 11. Total mean of (a) the radiosonde-derived LCL along the normalized path from
1127 California to Hawaii, (b) the equivalent potential temperature difference
1128 across the inversion, (c) the mixing ratio difference at the inversion, and (d)
1129 the potential temperature difference at the inversion along the normalized path
1130 from California to DE. Gray shaded region indicates interquartile range. The
1131 boxplot in (b) and (c) indicates the location of the maximum and minimum
1132 value near DE, the difference between the two is significant at 95% confident
1133 level.

1134

1135 12. The total mean (a) surface latent heat flux, and (b) surface wind speed along
1136 the normalized path from California to Hawaii. Gray shaded region indicates
1137 interquartile range.

1138

1139 13. (a) Profiles of medians of U wind difference of the composed U wind east of
1140 CB and that west of CB in the small region (solid black line) and in the large
1141 region (dashed black line); same for V wind difference in the small region
1142 (solid red line) and in the large region (dashed red line). Shaded area indicates

1143 interquartile range, and (b) MBLH along normalized path from California to
1144 Hawaii.

1145 14. MAGIC Instrument Status from Leg03A to Leg09B

1146 15. MAGIC Instrument Status from Leg10A to Leg18B

1147

1148

1149

1150

1151

1152

1153

1154

1155

1156

1157

1158

1159

1160

1161

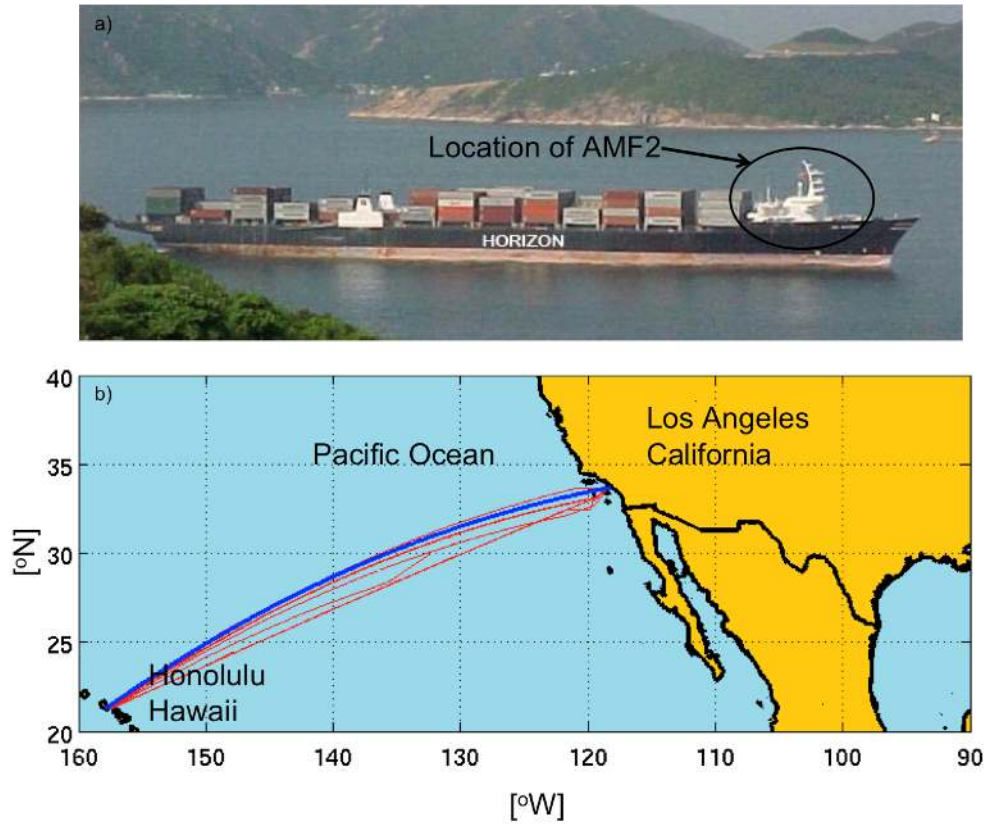
1162

1163

1164

1165

Figures



1166

1167

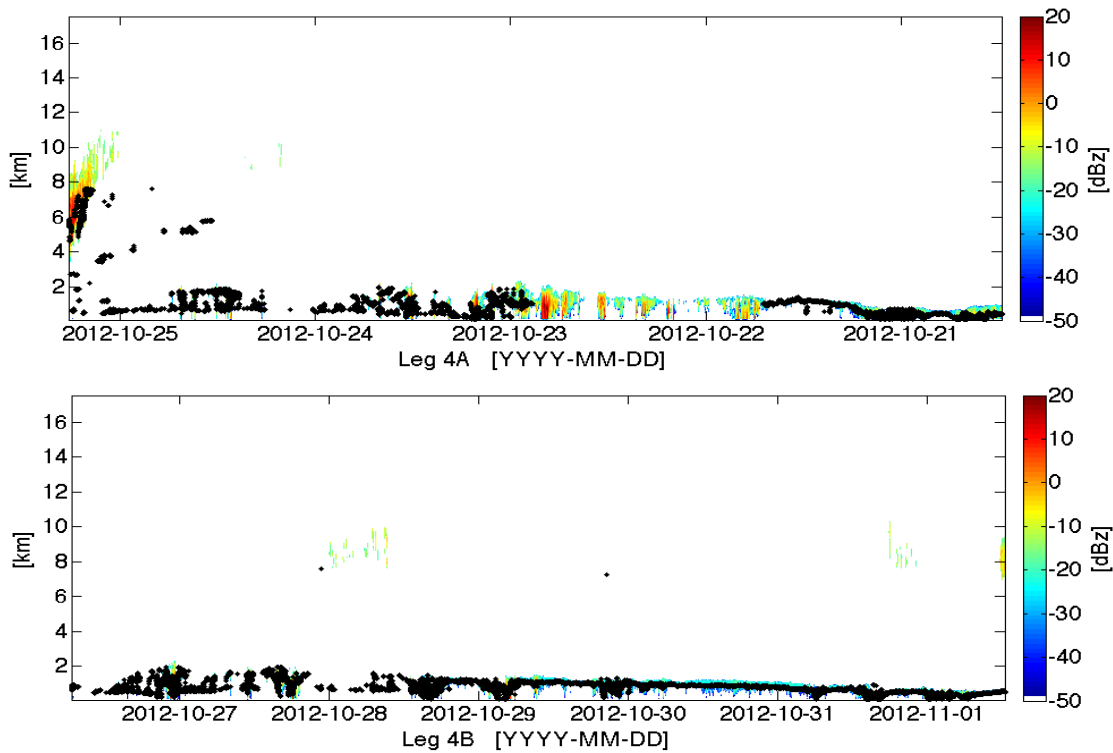
1168

1169

1170

1171

Fig. 1. (a) *Horizon Spirit* showing location of the bridge region where the AMF2 was located, and (b) Tracks of MAGIC legs between California and Hawaii (red lines) and great circle route (blue line).

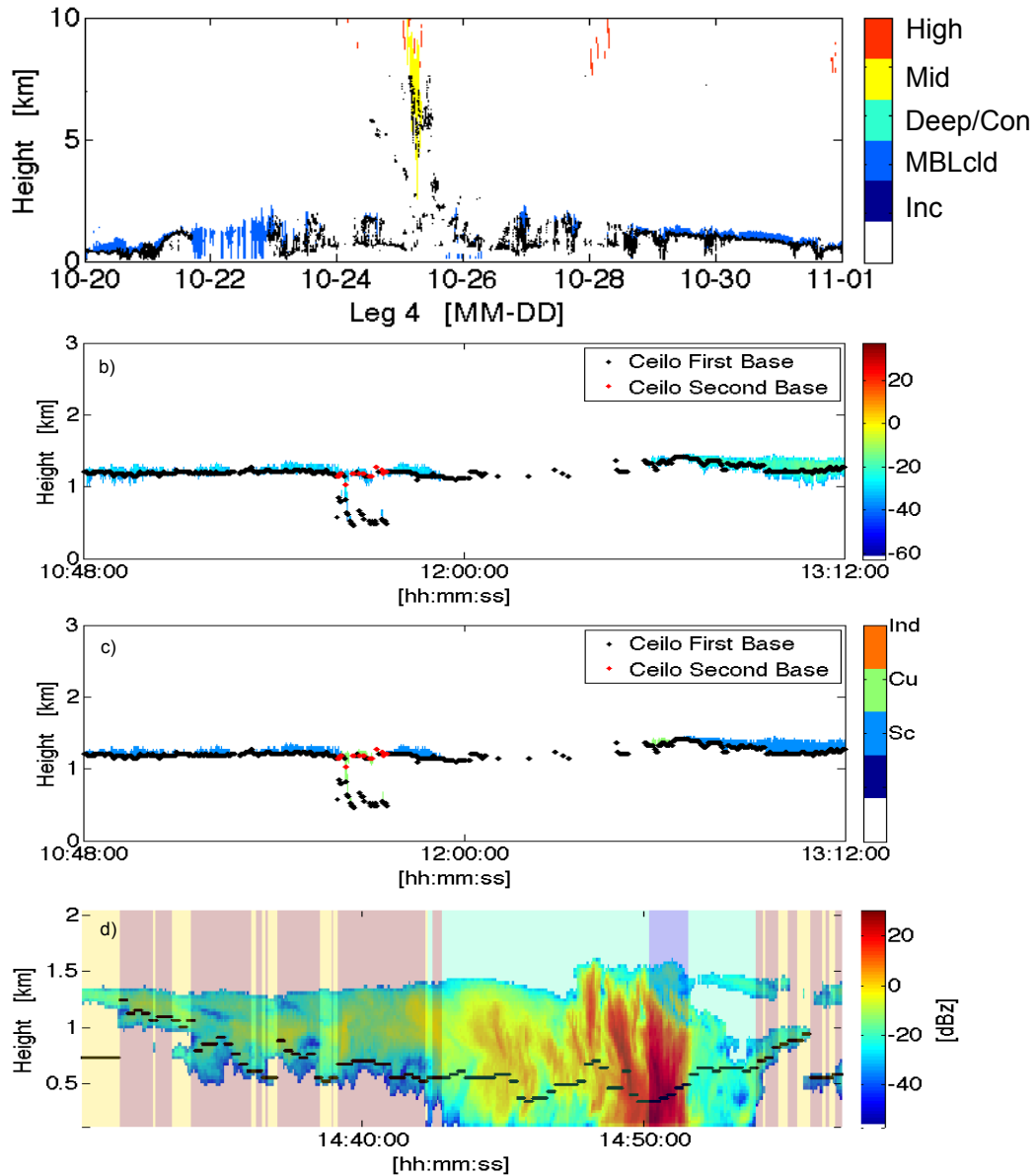


1173 Fig. 2. KAZR reflectivity observations for Leg04A (top panel) and Leg04B (bottom
 1174 panel) with the first ceilometer cloud base shown as black dots. The *Spirit* departed from
 1175 California on Oct. 21 (2012) and arrived in Hawaii on Oct. 25, then left on Oct. 26 and
 1176 returned to California on Nov. 1. Graphs are shown with Los Angeles to the right and
 1177 Honolulu to the left. The ceilometer data for 00:00 to ~21:16 UTC on Oct. 22, 2012 are
 1178 not available.

1179

1180

1181

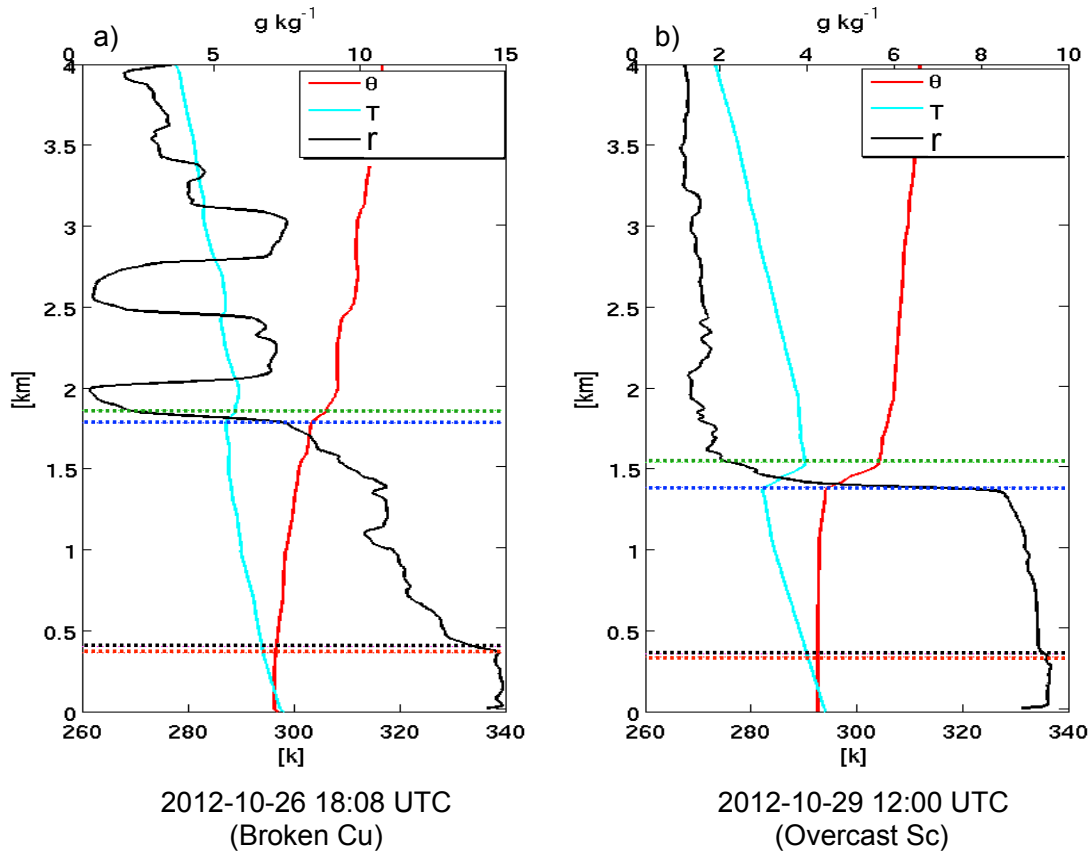


1182

1183 Fig. 3. (a) Cloud classifications for Leg04 with the first ceilometer cloud base shown as
 1184 black dots. The corresponding KAZR reflectivities can be seen in Fig 2. (b) KAZR
 1185 reflectivities with the first and second ceilometer cloud base shown as black and red dots
 1186 respectively for a short time segment on Oct. 21, 2012 during Leg04A. (c) MBL cloud
 1187 classifications with the first and second ceilometer cloud base shown as black and red
 1188 dots for the same time period as that shown in Fig. 3b during Leg04A. (d) KAZR

1189 reflectivities with the first ceilometer cloud base shown as black dots for a short time
1190 period on Oct. 28, 2012 during Leg04B. The pink, light blue and purple backgrounds
1191 indicate the occurrence of virga, MBL drizzle, and heavy MBL drizzle, respectively; the
1192 yellow background indicates no precipitation during that time period.

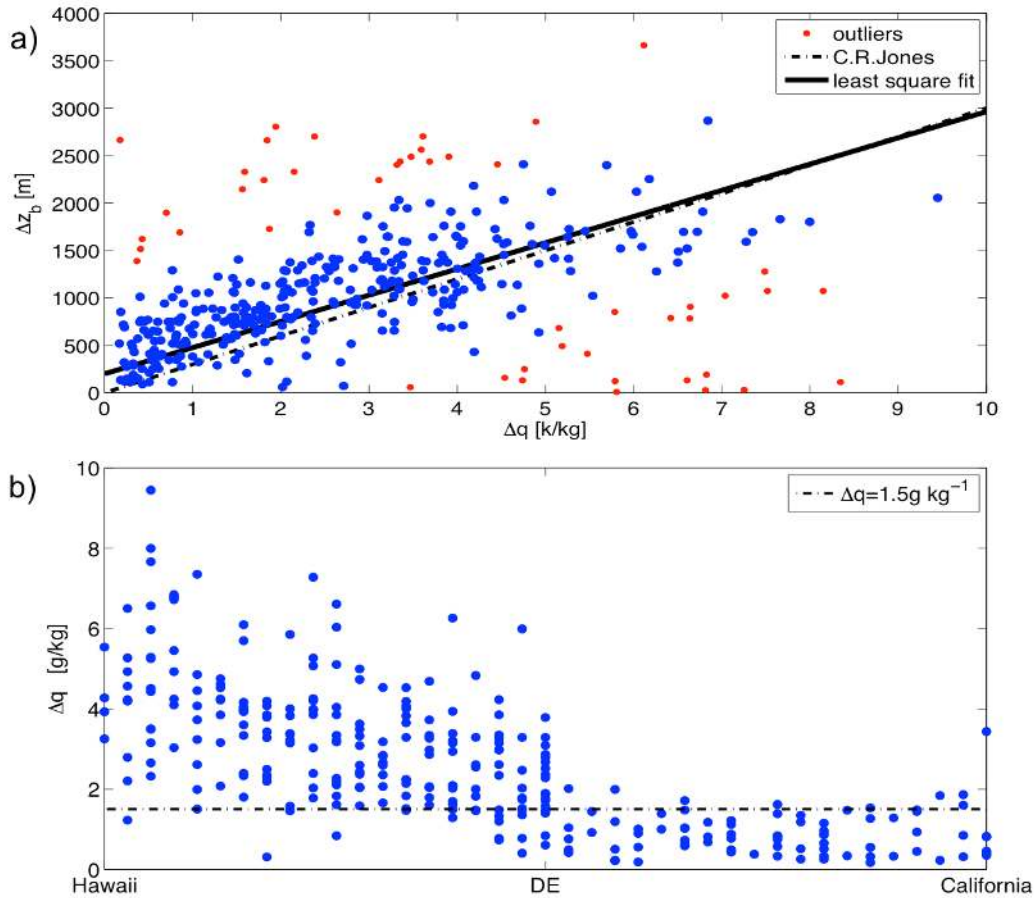
1193



1194

1195

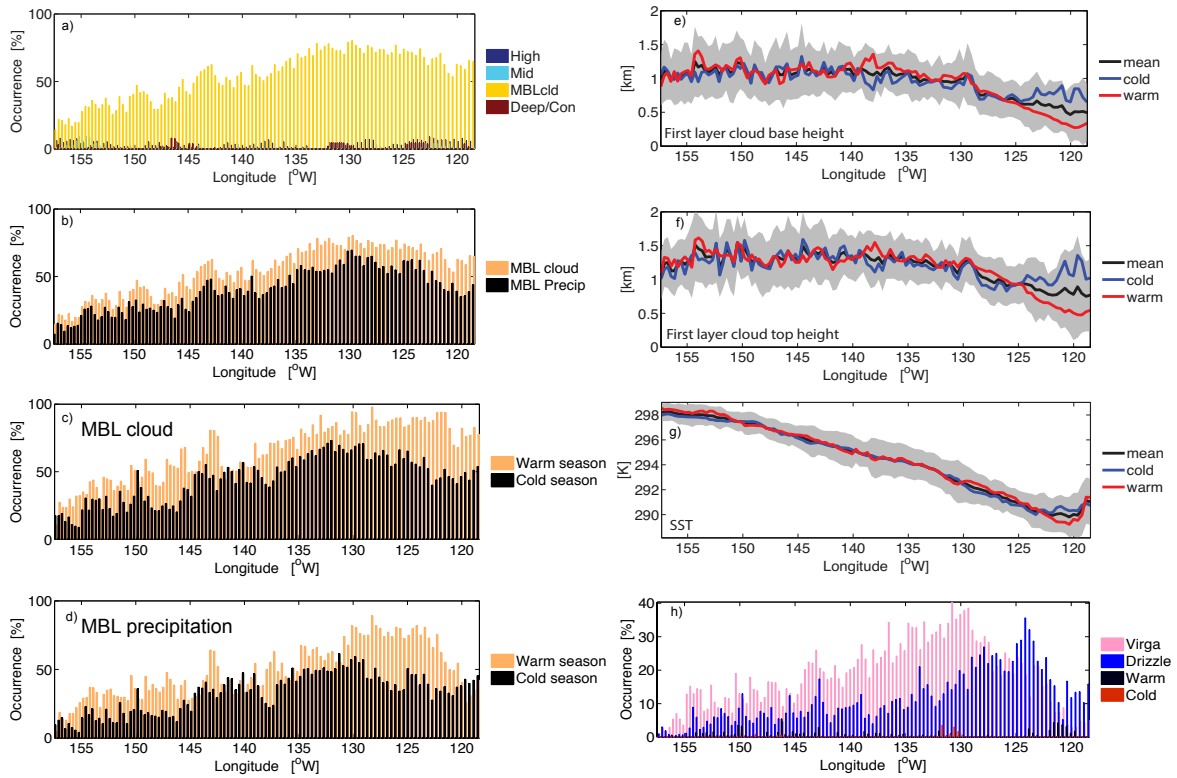
1196 Fig. 4. Profiles of temperature (T), potential temperature (θ), and mixing ratio (r) from
 1197 soundings. Green and blue dashed lines show the inversion tops and bases, while black
 1198 and red dashed lines show the transition tops and bases. (a) Sounding launched at 18:08
 1199 UTC, October 26, 2012, with broken Cu overhead. (b) Sounding launched at 12:00 UTC,
 1200 October 29, 2012, with overcast Sc overhead.



1201

1202 Fig. 5(a) The scatter plot of radiosonde-derived Δq for all the legs and maximum Δz_b
 1203 within four degrees longitude surrounding each radiosonde. The solid black line is the
 1204 least square fit with slope 276 m kg g^{-1} and intercept 200m . The dashed black line
 1205 represents the thermodynamic argument derived in Jone et al 2011. The red dots indicate
 1206 outliers outside 1.5 standard deviation of the least-square fit. (b) Radiosonde-derived Δq
 1207 for all the legs along the normalized path from California to DE to Hawaii.

1208

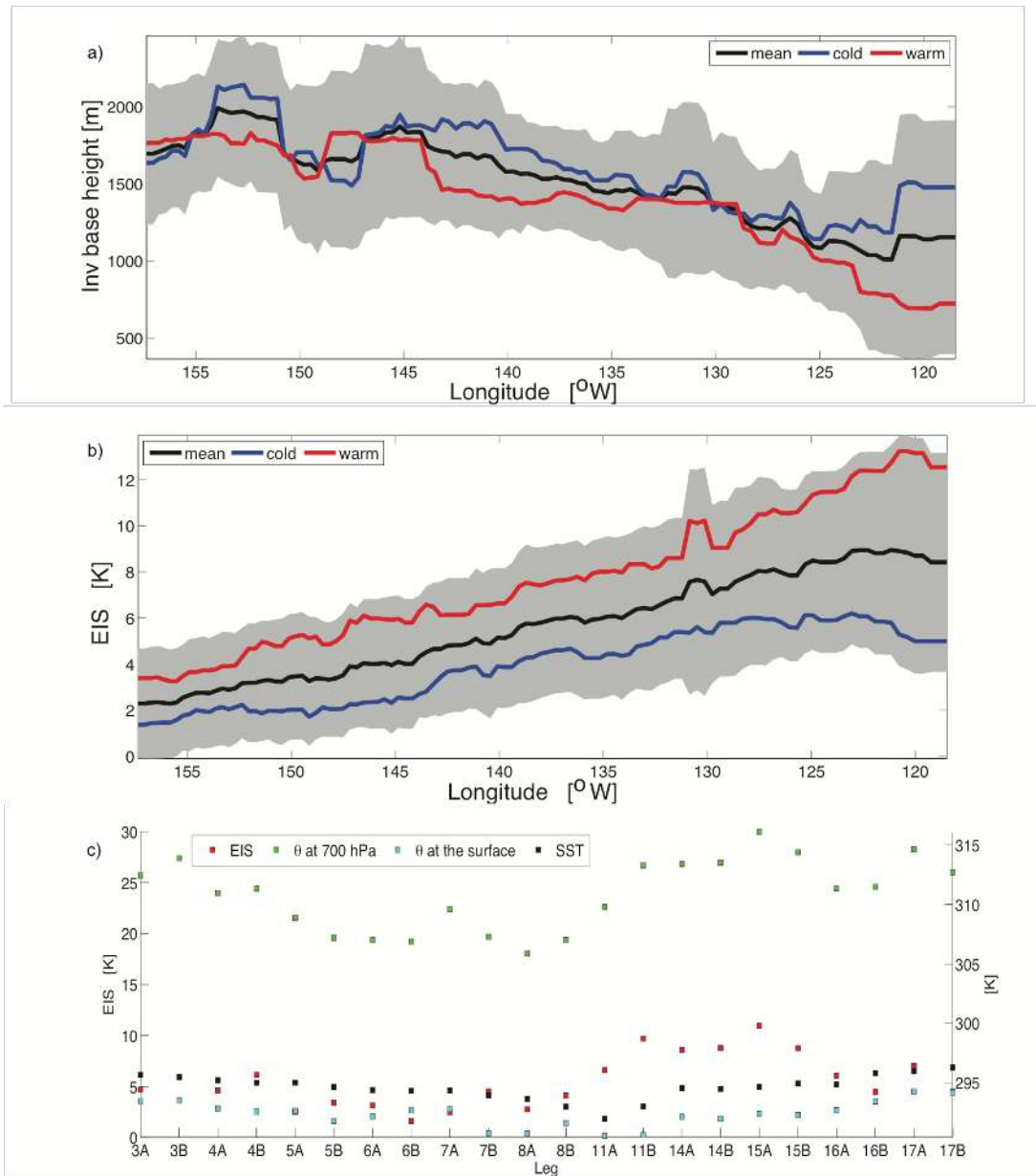


1209

1210 Fig. 6. Frequencies of occurrence along the MAGIC transect of (a) the four main cloud
 1211 types, (b) MBL clouds and observed MBL-cloud liquid precipitation, and (c) MBL
 1212 clouds and (d) observed MBL-cloud liquid precipitation during the warm and cold season
 1213 during the warm season (Leg11, Leg14-Leg17: May 25 -June 6, 2013, July 7-Aug. 29,
 1214 2013) and during the cold season (Leg03-Leg08: Oct. 6-Dec. 27, 2012). Total and
 1215 seasonal mean along the MAGIC transect of (e) first cloud base heights, (f) first cloud top
 1216 heights, and (g) SSST. The black line shows the total mean, the blue and the red line
 1217 shows the mean for cold and warm season respectively. The gray shaded region indicates
 1218 one standard deviation of the mean. Frequencies of occurrence along the MAGIC transect
 1219 of (h) liquid precipitation types.

1220

1221



1223

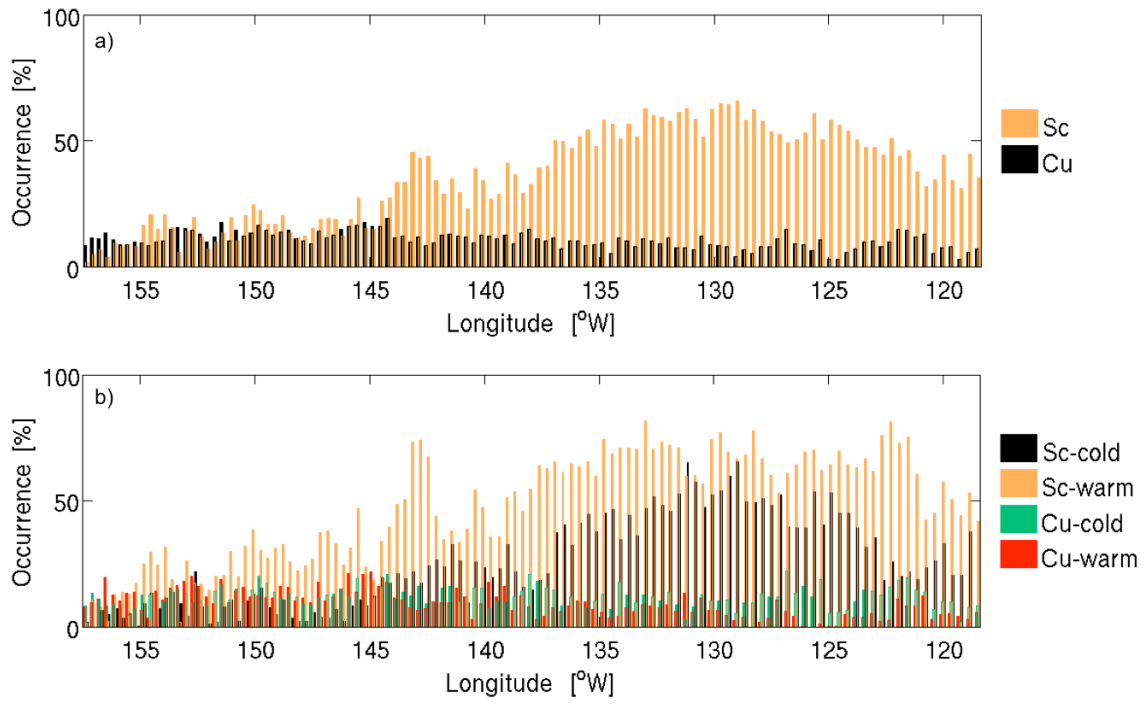
1224 Fig. 7. Total and seasonal mean of (a) MBLH, and (b) EIS along the MAGIC transect.

1225 The gray shaded region indicates one standard deviation of total. The black line shows

1226 the total mean, the blue line shows the mean of the cold season, and the red line the mean

1227 for the warm season, and (c) Leg-mean values of EIS, SSST, potential temperature at 700

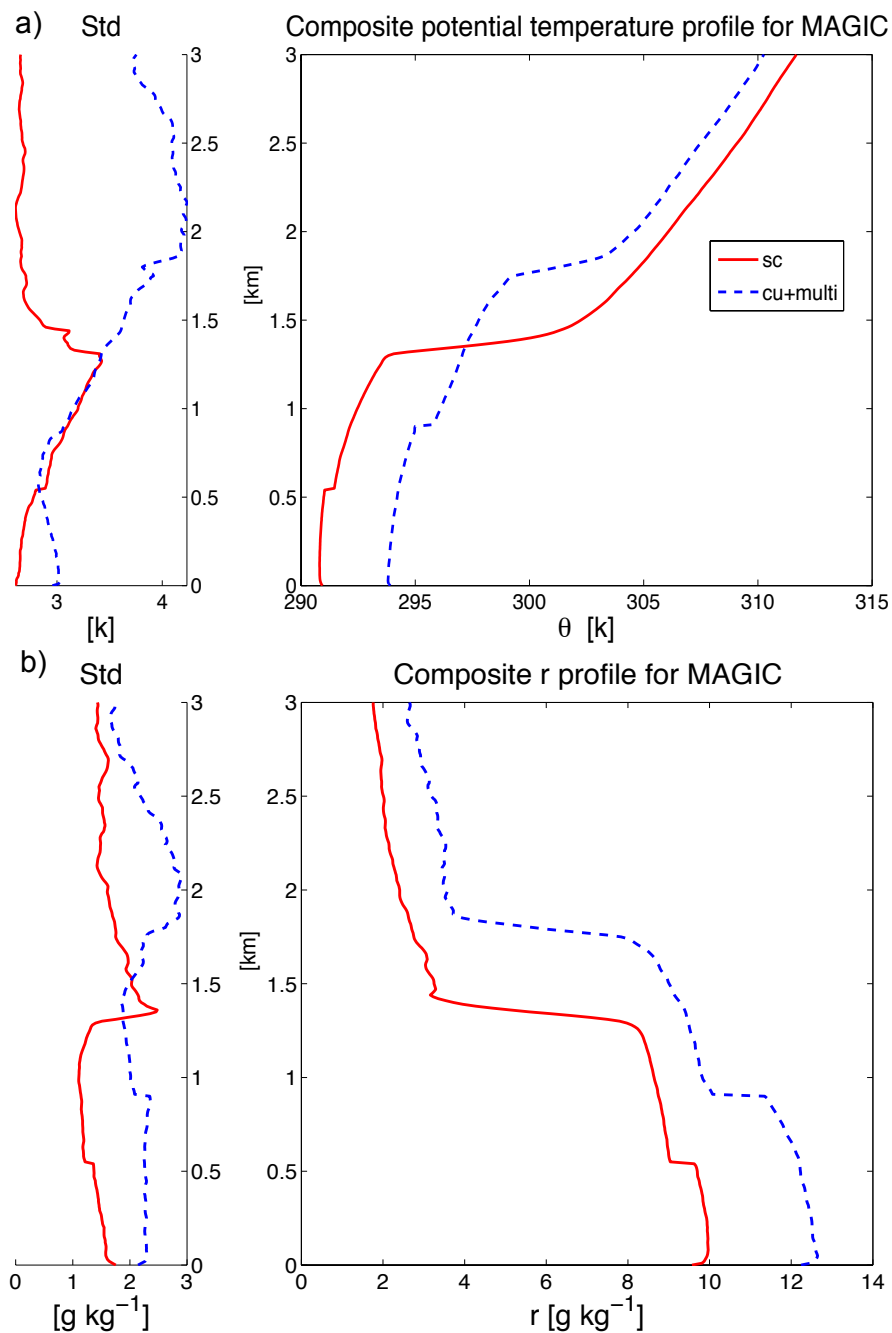
1228 hPa, and potential temperature at the surface.



1229

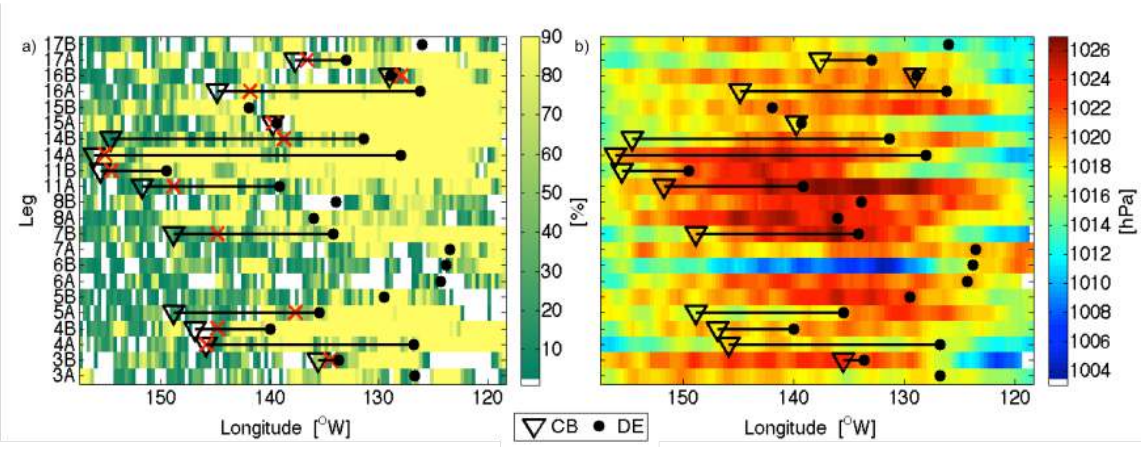
1230 Fig. 8. Frequencies of occurrence of cloud types (a) over the entire deployment and (b)

1231 during the cold season and warm season.



1232

1233 Fig. 9. Profiles of means and standard deviations of (a) potential temperature and (b)
 1234 water vapor mixing ratio composed over the cases with single stratocumulus at the
 1235 inversion level (blue dotted line), and single cumulus at the transition level together with
 1236 multiple MBL clouds (red solid line), both of which must contain a transition layer.



1237

1238 Fig. 10(a) CF_{36} , (b) the sea surface pressure along the MAGIC transect for individual legs.

1239 The black triangle and the black dots indicate the cloud breakup points (CB) and the

1240 starting points of the MBL systematic decoupling (DE). The red crosses in (a) indicate

1241 the location when CF_{108} drops to below 50% before CB. White spaces in (a) denote times

1242 when CF_{36} was less than 10%, and those in (b) denote missing data.

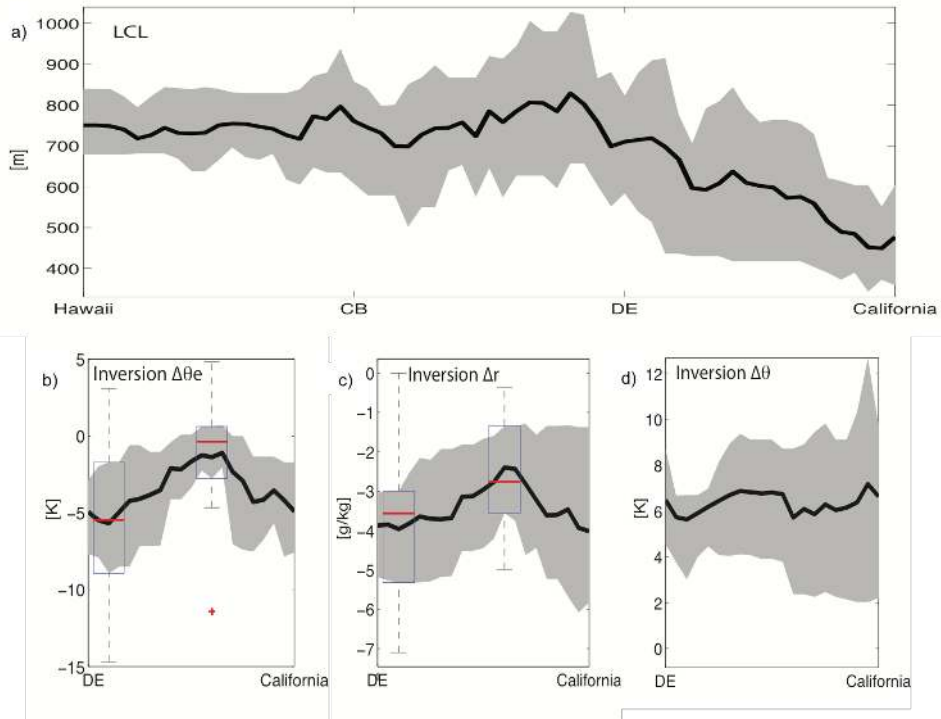
1243

1244

1245

1246

1247



1248

1249 Fig. 11. Total mean of (a) the radiosonde-derived LCL along the normalized path from
 1250 California to Hawaii, (b) the equivalent potential temperature difference across the
 1251 inversion, (c) the mixing ratio difference at the inversion, and (d) the potential
 1252 temperature difference at the inversion along the normalized path from California to DE.
 1253 Gray shaded region indicates interquartile range. The boxplot in (b) and (c) indicates the
 1254 location of the maximum and minimum value near DE, the difference between the two is
 1255 significant at 95% confident level.

1256

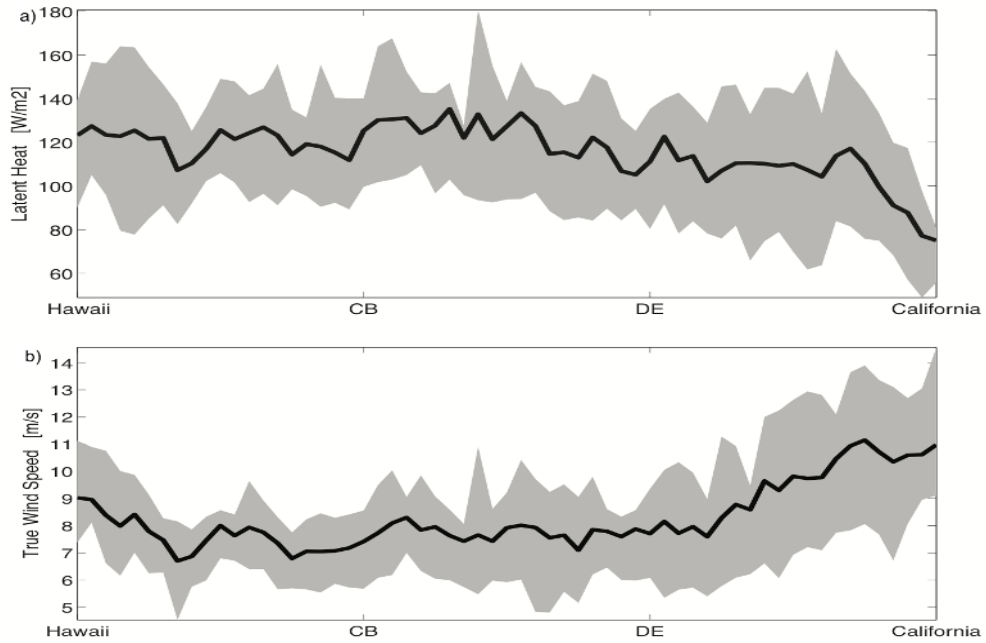
1257

1258

1259

1260

1261



1262

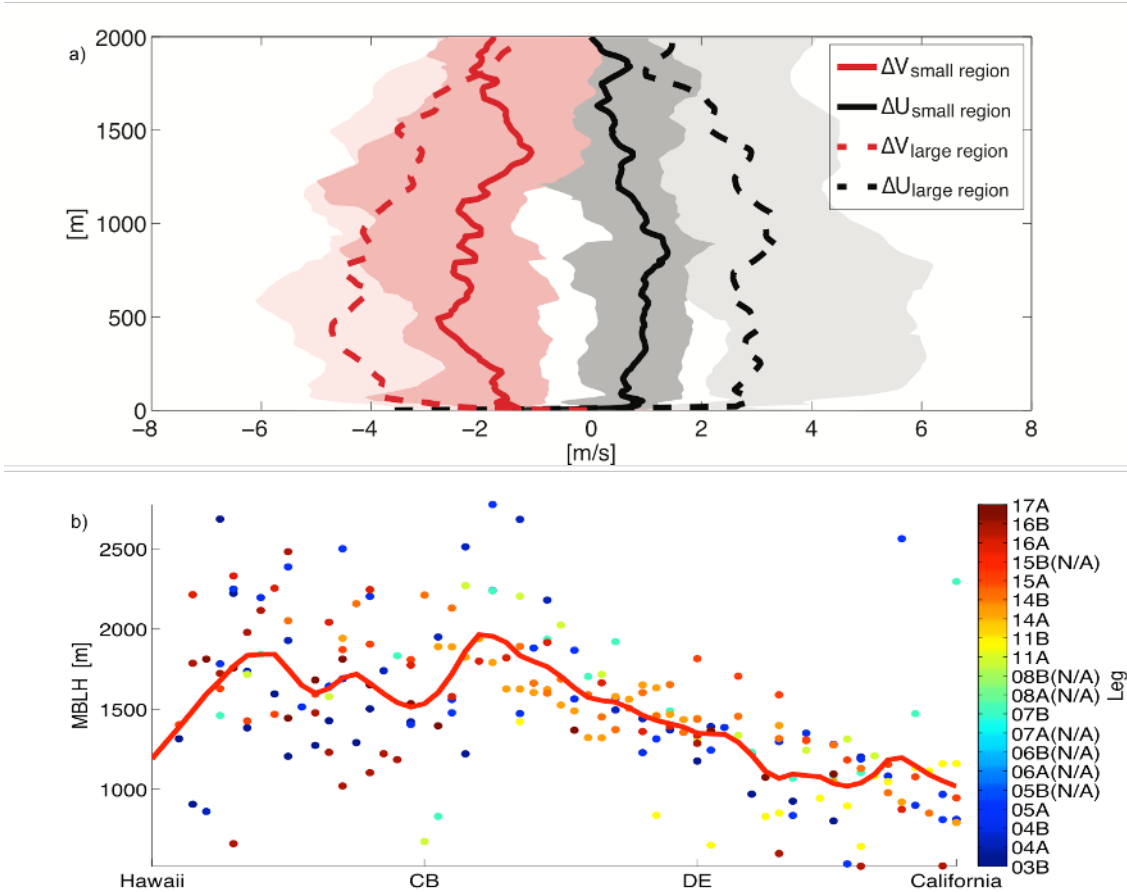
1263 Fig. 12 The total mean (a) surface latent heat flux, and (b) surface wind speed along the
1264 normalized path from California to Hawaii. Gray shaded region indicates interquartile
1265 range.

1266

1267

1268

1269



1270

1271 Fig. 13. (a) Profiles of medians of U wind difference of the composed U wind east of CB
 1272 and that west of CB in the small region (solid black line) and in the large region (dashed
 1273 black line); same for V wind difference in the small region (solid red line) and in the
 1274 large region (dashed red line). Shaded area indicates interquartile range, and (b) MBLH
 1275 along normalized path from California to Hawaii.

1276

1277

1278

1279

1280

1281

Instrument	Leg												
	03A	03B	04A	04B	05A	05B	06A	06B	07A	07B	08A	08B	09A
Ka-band reflectivity	Green	Green	Green	Green	Green	Green	Green	Green	Green	Green	Green	Green	Green
Ka-band spectra	Red	Green	Green	Green	Green	Green	Blue	Blue	Blue	Green	Green	Green	Green
W-band reflectivity	Black	Black	Black	Black	Green	Green	Green	Green	Green	Green	Green	Green	Green
W-band spectra	Black	Black	Black	Black	Green	Green	Blue	Blue	Green	Green	Green	Green	Green
Radar wind profiler	Black	Black	Black	Black	Black	Black	Black	Black	Yellow	Blue	Green	Green	Green
HSRL	Black	Black	Black	Black	Black	Black	Black	Black	Black	Black	Black	Black	Black
Multipulse lidar	Red	Red	Red	Red	Green	Green	Green	Green	Red	Red	Green	Green	Green
MWR 2-channel	Green	Green	Green	Green	Green	Green	Green	Green	Green	Green	Green	Green	Green
MWR 3-channel	Green	Green	Red	Red	Red	Red	Blue	Green	Green	Green	Green	Green	Green
ASSIST	Blue	Green	Green	Green	Green	Yellow	Yellow	Yellow	Green	Green	Green	Green	Green
Total Sky Imager	Red	Red	Green	Green	Green	Green	Green	Green	Blue	Green	Green	Green	Green
Ceilometer	Green	Green	Green	Green	Green	Green	Green	Green	Green	Green	Green	Green	Green
Portable Radiation Package	Green	Green	Green	Green	Green	Green	Green	Green	Green	Green	Green	Green	Green
Microtops readings	Green	Green	Black	Black	Black	Black	Black	Black	Black	Black	Black	Black	Black
CIMEL sun photometer	Black	Black	Black	Black	Black	Black	Black	Black	Black	Black	Black	Black	Black
Solar Array Spectrophotometer	Blue	Green	Green	Green	Green	Green	Green	Green	Green	Green	Green	Green	Green
Solar Spectral Flux Radiometer	Black	Black	Black	Black	Black	Black	Black	Black	Black	Black	Black	Black	Black
CPC	Green	Green	Green	Green	Green	Green	Green	Green	Blue	Green	Green	Green	Green
CCN	Green	Green	Green	Green	Green	Green	Blue	Green	Blue	Red	Yellow	Green	Green
UHSAS	Blue	Green	Green	Green	Green	Green	Green	Green	Blue	Green	Black	Black	Black
HTDMA	Blue	Green	Green	Green	Green	Yellow	Blue	Green	Blue	Red	Yellow	Black	Black
Wet/dry nephelometer	Blue	Blue	Green	Green	Green	Yellow	Yellow	Yellow	Yellow	Blue	Yellow	Yellow	Yellow
PSAP	Blue	Green	Green	Green	Green	Green	Blue	Blue	Green	Green	Green	Green	Green
Ozone	Green	Green	Green	Green	Green	Green	Blue	Green	Green	Green	Green	Green	Green
Aerosol sampling	Black	Black	Black	Black	Black	Black	Black	Black	Black	Black	Black	Black	Black
Navigational information	Green	Blue	Yellow	Green	Green	Yellow	Yellow	Yellow	Yellow	Green	Green	Green	Green
Meteorology	Green	Green	Green	Green	Green	Green	Green	Green	Green	Green	Green	Green	Green
Radiosonde launches	Green	Green	Green	Green	Green	Green	Green	Green	Green	Green	Green	Green	Green
Disdrometers	Green	Green	Green	Green	Green	Green	Green	Green	Green	Green	Green	Green	Green
IR thermometer	Red	Red	Green	Green	Green	Green	Green	Green	Green	Green	Green	Green	Green
ISAR	Green	Green	Green	Green	Green	Green	Green	Green	Blue	Green	Green	Green	Green

No issue
Corrective maintenance or partial data
Questionable data
Instrument down
Not in service

1282

1283 Fig. 14 MAGIC Instrument Status from Leg03A to Leg09B

1292

1293

1294